New modeling strategies for analyzing lateral-torsional buckling in class-4 steel structural members at elevated temperatures using beam-type elements

Myriam R. Pallares-Muñoz [a,b,*], Ignacio Payá-Zaforteza [a], Antonio Hospitaler-Pérez [a]

[a] *Universitat Politècnica de València, ICITECH, Camino de Vera S/N, 46022 València, Spain*
[b] *Universidad Surcolombiana, Cra 1 Aven. 26, 410010 Neiva, Colombia*

A B S T R A C T

Fire is one of the main hazards that can affect steel buildings and bridges and was responsible, e.g., for the collapse of the Plasco building in Tehran, Iran, and the I-65 bridge in Birmingham, Alabama, USA. This vulnerability has motivated the development of advanced computational models to predict the response of steel structures to fire accurately. The mechanical response of slender steel members to fire is especially important because they fail prematurely by buckling at load values below their elastic strength. However, the structural analysis of these members typically requires advanced and complex FE models with shell elements, including initial geometric and material imperfections. These shell models are computationally expensive, complicating the carrying out of parametric and probabilistic studies. Therefore, there is a need to develop simple, accurate, and low-cost computational models as reliable as shell-type models. To overcome this knowledge gap, this paper presents two new modeling strategies that simulate the mechanical response of class-4 steel members subjected to lateral-torsional buckling in fire using Timoshenko beam-type finite elements, which significantly simplify the structural modeling. These strategies are called Fiber Beam Model (FBM) and Cruciform Frame Model (CFM) and include initial geometric and material imperfections and thermal strains. In the FBM, the steel member is represented by a single fiber of I-section beam elements, whereas in the CFM, a cruciform arrangement of rectangular beam finite element fibers idealizes it, making the CFM more complex to build than FBM. Both strategies were satisfactorily validated with experimental and numerical results of Test-1 and Test-3 carried out in the "Fire design of steel members with welded or hot-rolled class-4 cross-section" (FIDESC4) research project on a slender beam of class-4 section. Although both FBM and CFM correctly captured the LTB resistance of the tested beam, CFM can, in addition, adequately reproduce the local buckling failure and significantly reduced the computational time. That means complex fire engineering problems such as probabilistic and optimization analyses of thin-walled beams can be addressed more easily and accurately, representing an important step towards applying performance-based approaches in slender steel structures under fire.

1. Introduction

Current requirements for building structures and large-scale roadway structures, such as bridges, are becoming increasingly demanding, requiring elements of larger dimensions that make them more costly [1]. On the other hand, current trends in the construction of large-scale projects have made steel structures a major construction alternative [2]. The inevitable need to optimize costs under allowable performance levels has greatly interested in using lighter sections. Recent cases demonstrated it. For example, in the Wirkowice bridge in Poland (2020), hot-rolled high-strength lightweight steel sections were used to reduce the weight and increase the bridge span [3]. Another illustrative case is Chicago's Union Station Tower (2020). In this 51-floor office steel building, designers reduced the total structural steel in the upper perimeter columns by almost 20% using stronger but lighter steel elements (552 MPa), creating more open space in upper floors [4].

However, the decrease in the amount of material in the fabrication of steel members to make them lighter also makes them slenderer. That condition may compromise the structure's stability because of the possible activation of global or local buckling failure phenomena that, in practice, are more critical when the structure is in a fire situation [5]. Examples of such failures have been observed in buildings (e.g., the

2001 fire in New York City's World Trade Centre 7 [6,7] or the 2017 fire in Tehran's Plasco building [8,9]) and bridges (e.g., the I-65 overpass fire in Birmingham, Alabama, USA [9] and similar cases reported in [10–14]).

The trend towards cost-benefit optimization has led to increasing the use of lightweight and slender sections classified by Eurocode as class-4 [15] in construction projects. Class-4 cross-sections are those in which local buckling will occur before attaining yield stress at any cross-section point because its parts have a minimal thickness compared to the width [16]. Therefore, the analysis is limited to the elastic range (see Fig. 1, which illustrates the ideal plastic behavior achieved for compact class-1 and class-2 sections but not for the non-compact class-3 and slender class-4 sections). These welded or hot-rolled class-4 cross-sections usually are built to safely cope with possible Lateral-Torsional Buckling (LTB) phenomena in beams and flexural buckling in columns at room temperature [17,18]. However, it is also essential to know the performance of these sections when the adverse effects of imperfections and fires are present [5] because they may compromise the stability of the structure and, ultimately, its safety.

The Geometrically and Materially Non-linear Mechanical Analysis with Imperfections (GMNIA, henceforth) is the most advanced and accurate method to solve the LTB problem in steel members [20]. GMNIA can predict the structural member critical loads considering local and global buckling failures (buckling loads), which can appear even before the cross-section plastifies, and define the actual load-bearing capacity of the member [21,22]. The geometrical nonlinearity in the GMNIA is due to large displacements, which are especially important under fire. The material nonlinearity is caused by the creep and the elastoplastic behavior of steel. The imperfections of welded class-4 cross-section steel members come from geometrical and material defects appearing in the plate fabrication process and later in the cut and welding process [23]. Geometrical imperfections can be measured on trajectories along the flange and web plates of the steel member. They can then be drawn to define longitudinal imperfection profiles that approximate the imperfect shape of the flanges and web [24]. These imperfection profiles resemble sinusoidal shapes and provide an approximated idea of the number of undulations in a steel member area. The measured amplitude is the maximum imperfection value of the profile. For modeling purposes, the assumed shape of the initial global and local geometric imperfections can be obtained from combining elastic buckling mode shapes. This method enables the calculation of the amplitude of imperfections in slender steel members [25]. On the other hand, structural (or material) imperfections in steel members with class-4 cross-sections are caused by the high temperatures applied in the welding process that induce a state of residual stresses that remains in the whole section of the unloaded member, even after cooling [23]. Thus, these residual stresses are present before beam loading as an initial condition at room temperature in the modeling.

Several numerical studies have considered that the increase of temperatures in steel members caused by fires relaxes the residual stresses
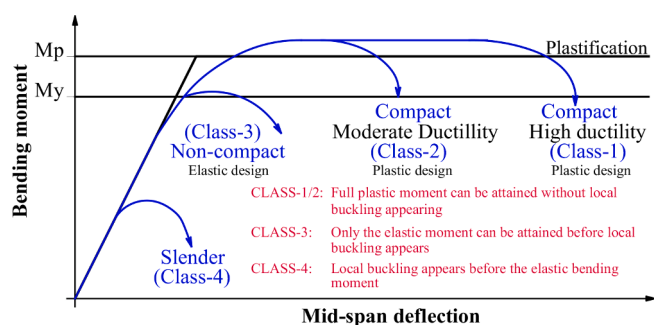

Fig. 1. Moment-deflection relationship for a simply supported steel beam according to cross-section class. Adapted from [19]. M_y is the cross-section elastic bending moment, and M_p is the cross-section plastic moment.

and makes its influence on failure loads small or even neglectable. For example, in a study for predicting the plastic capacity of axially loaded steel beam columns with thermal gradients, Quiel et al. [26] did not consider residual stresses in the computational models because it was assumed that these stresses relaxed due to increasing steel temperature. In an experimental study of the strength of wide flange columns at elevated temperature, Yang et al. [27] concluded that the initial residual stresses affected significantly less the local and global buckling failure modes in fire situations than at room temperature. Heidarpour and Bradford [28] showed similar results in a separate parametric computational study of the effects of residual stresses in heated steel members. The initial LTB numerical models of class-4 tested beams under bending carried out in the "Fire design of steel members with welded or hot-rolled class-4 cross-section" (FIDESC4 henceforth) research project [24] neglected thermal expansion as well as residual stresses [26]. However, Couto et al. [29], in a later study based on the LTB results of FIDESC4, concluded that residual stresses negatively influence the LTB strength under fire of beams with slender cross-sections with LTB strength reductions under fire of a maximum of 15%.

Practically all of the LTB numerical simulations of slender section steel members under fire have used models with shell elements (see, e.g., those of the FIDESC4 report [24] and later works based on the FIDESC4 test results [30–33] as well as other LTB assessment of steel beams included in [34,35]). Nguyen and Park [36] also used shell elements in numerical simulations to evaluate the LTB resistance of steel H-beams exposed to a localized fire considering the combined effects of initial geometric imperfections and residual stresses. Kucukler [37] used shell elements to study LTB in steel beams not susceptible to local buckling, without local imperfections, and under the combined effects of fire and a constant bending moment. Based on the results of an extensive parametric study, Kucukler [37] also proposed an equation for the LTB assessment, which can only be applied to steel beams with class 1 and 2 cross-sections because only global buckling was studied.

Typical shell models naturally capture buckling (local and global) in slender steel section members but at high modeling and CPU time costs, making them difficult to use in parametric and probabilistic studies [38]. Thus, it is necessary to devise simpler beam-type models as reliable as shell-type models to carry out these analysis types at lower costs. This type of model has eventually been used in the bridge deck analysis. For example, Hambly [39] explains the use of grillages and space frames to calculate bridge decks subjected to bending, shear, and torsion. In these methods, the structure is represented by equivalent beam elements. Following this trend, some LTB simulations have been carried out using beam-type finite elements. Quiel et al. [26] evaluated the fire response of beam-columns with an I-section subjected to flexural compression under non-uniform temperature gradients with a fiber model of beam elements without including global imperfections and residual stresses, finding a good correlation with the experimental results. These researchers concluded that the added computational cost and complexity of a shell model were unnecessary to predict fire-exposed behavior when the failure mode is entirely plastic. Smyrnaios et al. [40] applied an Equivalent Truss Model proposed in [39,41] to determine the LTB resistance of I-section beams at room temperature. The Truss Model idealizes the beam through an equivalent system where two T-sections represent the upper and lower third parts of the beam connected through X-bracing truss elements representing the remaining part of the web. This technique was satisfactorily verified at room temperature with shell models through a parametric study for different geometric imperfection levels. Still, it was not validated with experimental results and was not tested at high temperatures. The Truss Model disadvantage is the impossibility of including the residual stresses in the X-bracing elements, which are naturally present in localized zones of the I-section. Possidente et al. [42] developed a 3D-beam finite element for modeling the fire behavior of open cross-section steel elements subjected to torsional effects. Displacement predictions in the LTB behavior of an L-frame carried out with a typical beam discretization model indicated a good

agreement with shell-based models if local buckling, residual stresses and imperfections are not present. This work does not contain any validation of the 3D-beam element with experimental results and local buckling was not considered. Franssen et al. [43] proposed an effective stress-based method for slender steel members exposed to high temperatures, which was implemented on fiber-type beam finite elements in SAFIR. This model is a constitutive law of steel that considers the local instabilities in slender steel sections in numerical models based on Bernoulli finite beam elements. The method was validated against experimental results from three FIDESC4 column tests at high temperatures [24]. The validation of the results was satisfactory, although conservative. Maraveas et al. [44] refined the methodology and revised some assumptions [45–47] to improve the original model proposed by Franssen et al. [43]. As a result, they developed an equivalent law to be used in the nonlinear numerical analysis of the fire resistance of thin-walled steel members. The constitutive model was implemented in SAFIR and validated against experimental results of columns subjected at elevated temperatures (FIDESC4 Test-3 [24] and others column tests reported in [48]). Although the simulation results revealed good agreement with the tests, the improved model still gave conservative results for large compressive load eccentricities, so the model is currently still under development.

Within this context, this study proposes two new modeling strategies based on beam-type elements that reduce the high modeling and analysis time costs of shell models typically used to carry out the GMNIA analyses to determine the strength of class-4 steel members. These modeling strategies use 7-DOF second-order Timoshenko beam finite elements (ANSYS BEAM189) and include: a) geometrical and material nonlinearity, b) thermal strains, c) Poisson effect on the cross-section owing to mechanical and thermal loading (i. e., the cross-section is scaled as a function of axial stretch), d) imperfections and residual stresses as initial conditions, e) non-uniform temperature, f) preliminary thermal conditioning (perturbed shape and additional thermal stresses), g) self-weight, h) non-linear stabilization of non-linear buckling and post-buckling solution. The first strategy is called the Fiber Beam Model (FBM) and uses a single fiber of I-section BEAM189 elements located at the center of the bottom flange to represent the steel member. The second strategy is called the Cruciform Frame Model (CFM) and idealizes the steel member with a cruciform grid of fibers, where rectangular BEAM189 finite elements make up each fiber. The CFM grid provides flexibility and enables capturing local buckling.

These new numerical strategies are validated using the test results (Test-1 and Test-3) of the FIDESC4 research project reported in [24] conducted with built-up welded steel beams with class-4 cross-sections heated and loaded until LTB failure. To get additional information about the accuracy and advantages of the proposed strategies, a full GMNIA of a shell model of both tests, including the application of residual stresses as zero state, imperfections, and thermal strains, were also carried out in ANSYS. The numerical results and computational times of these shell models were compared with those of the FBM and CFM to analyze the performance of the proposed modeling strategies. In addition, FMB and CFM without residual stresses and thermal strains were also carried out to evaluate how the LTB response of the tested beams is affected by not including these two initial conditions.

The paper is structured as follows: Section 2 describes the setup of the FIDESC4 Test-1 and Test-3 used to validate the proposed modeling strategies; Section 3 presents the FBM and CFM modeling strategies; Section 4 presents the implementation of the GMNIA in the FBM and CFM strategies; Section 5 presents the validation of the two strategies with experimental and numerical results of FIDESC4 Test-1 and Test-3. Section 5 also includes the numerical results of Test-1 and Test-3 simulations with the modeling strategies without residual stresses and thermal strains and their comparisons with those having them and some further important analyses of the LTB phenomenon in the FBM related to warping, bimoment, and bicurvature. Finally, Section 6 details the main conclusions and future works of the investigation.

2. Description of the Fidesc4 tests used for validation

The results of two fire experiments on constant cross-section beams (Test-1 and Test-3 of the FIDESC4 experimental and numerical investigation of class-4 beams [24]) were used to validate the proposed modeling strategies. Therefore, this section describes the main features of these fire tests. Both experiments were carried out with slender, simply supported, built-up welded beams with constant cross-section representing structures with a class-4 cross-section (see Figs. 2 and 3 for a detailed geometrical definition of the tests). The beams spanned 5 m and were heated along the central part where the temperature was intended to be constant and uniform and then loaded until failure due to the local instability of the plates. The loading consisted of two equal concentrated loads applied symmetrically so that the bending moment in the central heated part was constant. Fig. 4 illustrates the test setup along with the ceramic pads used to heat the beam and the devices used to load it. Fig. 5 exemplifies the tested beam subjected to pure bending in the central heated zone.

Before the tests, the steel properties of the beam plates were obtained at room temperature (see Table 1). According to EN 1993-1-2 [16], the slenderness of the web plate was $\overline{\lambda}_p = 1.33$ for Test-1 and $\overline{\lambda}_p = 1.13$ at the middle span for Test-3 [24]. After placing the beams on the supports, laser scanning and manual measurements established the initial geometry with imperfections. For the measurement of the global imperfection amplitude, the deviation between the stiffeners was measured. In the central zone of the tested beams, local imperfections were measured on the web and the top flange. Local imperfections on the web were measured in points placed in the compression part. On the top flange, they were measured over the edges where the cut-off imperfections of the plates are expected to be higher. Then local imperfection profiles were drawn. The maximum values of these local imperfection profiles were assumed as the local imperfection amplitudes. Table 2 lists the amplitude of local and global imperfections for each test [24].

Fig. 6a shows the setup of the experiments. Point pinned supports were located at the end extremities of the beam, as shown in Fig. 6b and c. All rotations and transverse deflections between these point supports were allowed, except at the stiffener points where the lateral deflection was restrained. Displacements in all directions were restrained in the left support, while only the axial displacement was released in the right support. In addition, both supports allow free torsion of the end cross-section. The beam was heated with Manning heat power units and flexible ceramic pads (see Fig. 4). Temperatures were measured from the beginning of the heating to the end of the tests. For this purpose, thermocouples along the beam according to the position of the ceramic pads were distributed. Both tests were set to be at 450 °C. However, the measured temperatures slightly varied during the tests and were not uniform for the whole section. The average measured temperatures at each part of the beam (top flange, web, bottom flange) used for numerical modeling are shown in Fig. 7a. The load was applied through a hydraulic jack and introduced by a distributing beam at the edges of the heated central part, as shown in Figs. 4 and 6d. The two vertical load application points were laterally restrained by frames contacting the beam through gadgets, as shown in Fig. 6e. Four potentiometers were used to measure the displacements in the load application points and calculate the deflections in the bottom flange center and the lateral rotation of the beam at mid-span. The tests were deflection controlled with a vertical deflection rate of 3.5 mm per minute (see Fig. 7b). The final vertical deflection measured at mid-span at the end of the experiments was 50 mm [24].

3. Proposed modeling strategies

FIDESC4 investigation [24] used shell elements instead of beam elements in the numerical models because local buckling was one of the dominant failure modes, and it depends on localized residual stresses
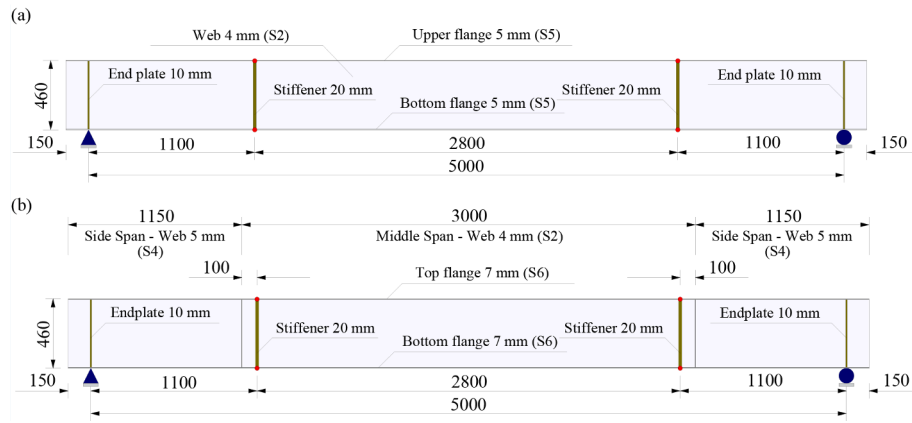
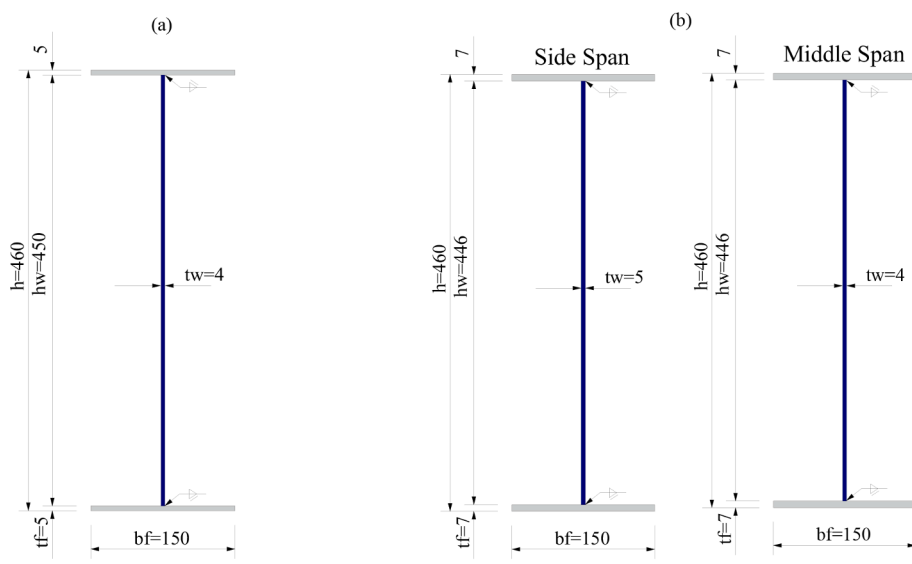**Fig. 2.** Dimensions and materials of tested beams. (a) Test-1. (b) Test-3 [24].

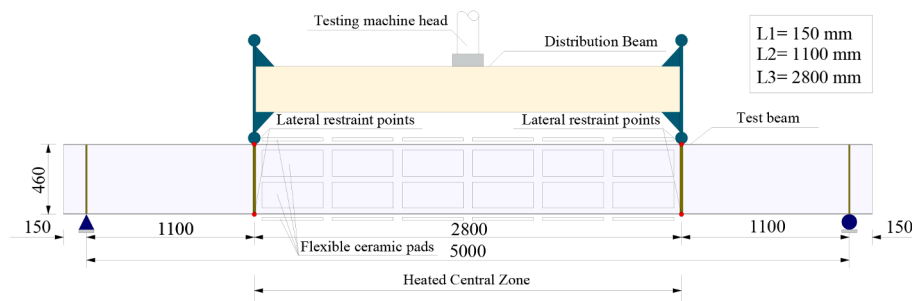**Fig. 3.** Dimensions of welded I-sections, in mm. (a) Test-1. (b) Test-3 [24].

Fig. 4. Scheme of the experiment (based on [24]).

and imperfections that are difficult to include in beam elements. However, this paper proposes two new modeling strategies to analyze class-4 beams subjected to LTB under elevated temperatures using ANSYS 3D beam finite elements. These modeling strategies are denoted by FBM (Fiber Beam Model) and CFM (Cruciform Frame Model). Both modeling strategies are made up of appropriate Timoshenko BEAM189 finite elements available in ANSYS. This finite element is three-node quadratic (see Fig. 8a), with seven degrees of freedom at each node: 3 translations (Ux, Uy, Uz), 3 rotations about the *x, y, z*-global directions (ROTx, ROTy, ROTz), and the warping magnitude to represent the cross-section

deformations due to high temperatures (WARP). Each section of the BEAM189 finite element is a predetermined set of cells with nine nodes and four integration points per cell (Fig. 8b). The number of cells influences the accuracy of the geometric and material properties and the ability to model the non-linear stress–strain relationship in the element cross-section. The calculations of the material inelastic behavior and the section temperature variation are performed at the section integration points. The element supports uniform temperatures and thermal gradients that vary linearly in the two cross-section directions and throughout the element [49]. BEAM189 also has a great capacity for static and
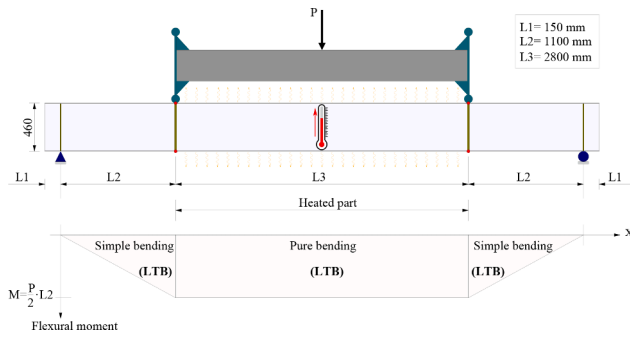
Fig. 5. Tested beam subjected to pure bending (based on [24]).

Table 1
Steel properties at room temperature [24].

Test/Part of beam	Steel samples	Average Yield Stress (MPa)	Elastic Modulus (MPa)
Test-1/Web Test-3/Web middle span	S2	392.8	176,897
Test-1/Flanges	S5	381.5	209,988
Test-3/Web side span	S4	368.5	199,200
Test-3/Flanges	S6	421.5	208,900
Stiffeners	—	355.0	210,000

Table 2
Amplitudes of local and global imperfections, in mm [24]

Imperfection	Test-1	Test-3
Local (Top flange)	2.27	0.69
Local (Web)	7.36	5.80
Global	2.50	1.50

dynamic geometrical and material non-linear analysis, suitable for solving stability problems (buckling, post-buckling, and collapse). The Timoshenko theory of the BEAM189 element assumes a shear-state in the cross-section (not present in Euler-Bernoulli theory). This assumption better approximates the cross-section deformation in deep beams, which is considered important given the great relevance of shear effects in fire-affected beams, where the material behaves as heterogeneous due to the effects of high temperatures on the steel mechanical properties [38,50], as it is in the present case study. Results such as deflections at the pseudo-mesh of the BEAM189 finite element cross-section are calculated in the post-processing stage from the node results and can be shown in extruded views.

In the FBM, the tested beam is discretized as a fiber (see Fig. 9a) of I-section BEAM189 elements. In the CFM, the beam is represented as a cruciform arrangement of fibers (see Fig. 9b) to make the model more flexible with a greater number of degrees of freedom and thus be able to emulate the behavior of a model with shell elements at a lower computational cost, taking advantage of the extrusion of the BEAM189 element. CFM can also be understood as a grid of rectangular BEAM189 elements capable of reproducing the local buckling failure. In FBM, non-linear LINK180 compression truss elements are additionally included, just where the stiffeners are located, to reproduce the three-dimensionality of the test and the boundary conditions. In CFM, end-plates and stiffeners are vertical fibers of rectangular BEAM189 elements, and boundary conditions can be easily applied to the model nodes.

4. LTB-GMNIA of the tested beams

The LTB problem of the beam with class-4 cross-section in fire is solved through a GMNIA in ANSYS, including a linear buckling analysis and the imperfection amplitudes measured to introduce the initial imperfections. GMNIA also involves non-linear buckling and post-buckling analyses. Non-linear buckling analysis is a static analysis with large deflections active, extended to a point where the beam attains its limit load or maximum load, including the material nonlinearity. Meanwhile, the post-buckling analysis is a continuation of the non-linear buckling analysis after the load attains its buckling value. A special non-linear stabilization technique is applied to overcome the local and global buckling instability problems due to the post-buckling stage is unstable [49]. Numerical instability matches the instability of the structure. When instability appears in the structure, large changes in displacements occur with only small load perturbations. ANSYS program uses an internal non-linear stabilization technique to solve the numerical instability by applying artificial dampers to the nodes with unstable degrees of freedom. A damping force is calculated proportionally to the pseudo velocity at these nodes, which is determined as the displacement increment divided by the pseudo time increment of the sub-step. For nodes with practically stable degrees of freedom, the influence of damping is negligible since the displacements and stabilization forces are relatively small compared to the physical forces. Although the stabilization forces (or damping factors) have the same unit and definition as the classical damping forces, the concept, in essence, is numerical and artificial for the calculation of non-linear stabilization [51]. The GMNIA steps applied in the FBM and CFM strategies are outlined below, followed by an explanation of each step.

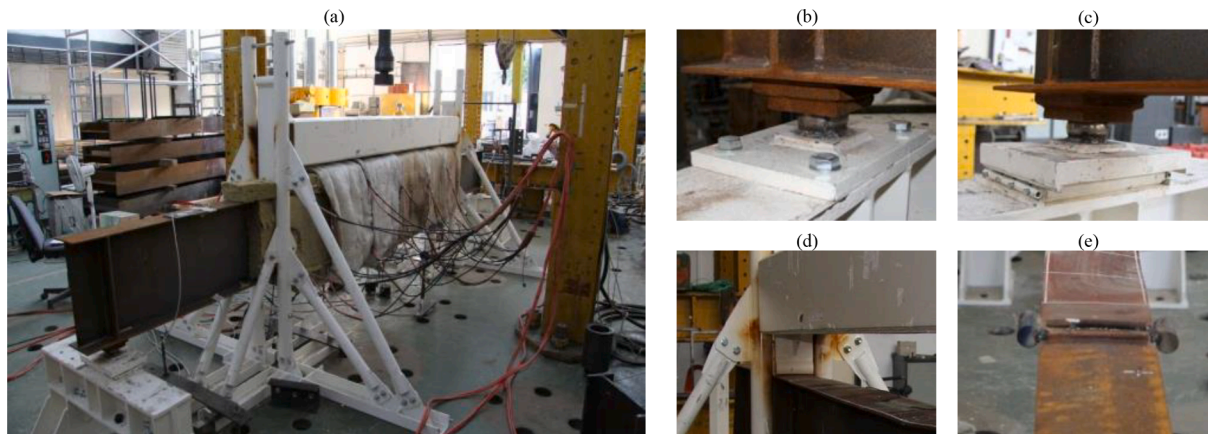1. Finite element model definition. Creation of the model and boundary conditions.

Fig. 6. (a) Test setup. (b,c) Pinned supports. (d) Application of load through a distribution beam. (e) Gadget on beam for lateral restrain [24].
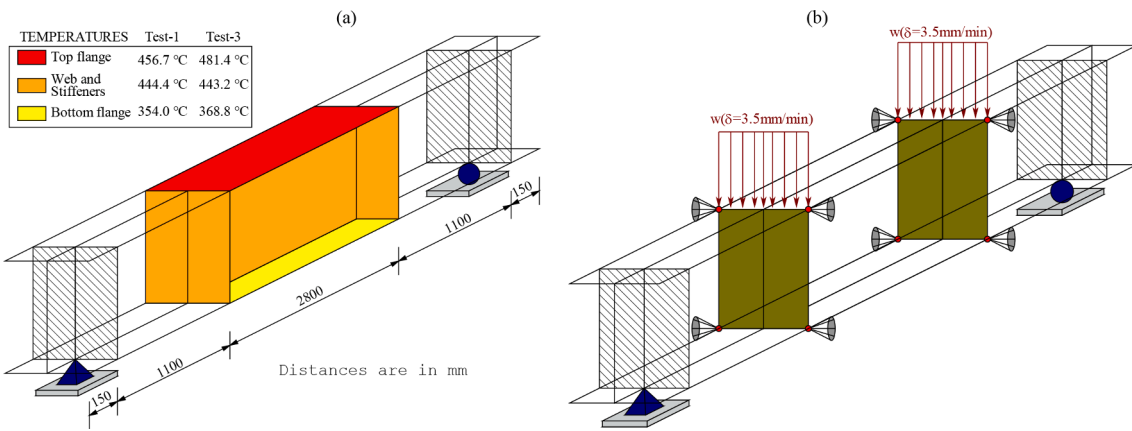
Fig. 7. (a) Average steel temperatures in the heated zone of the beam. (b) Test boundary conditions and loads.
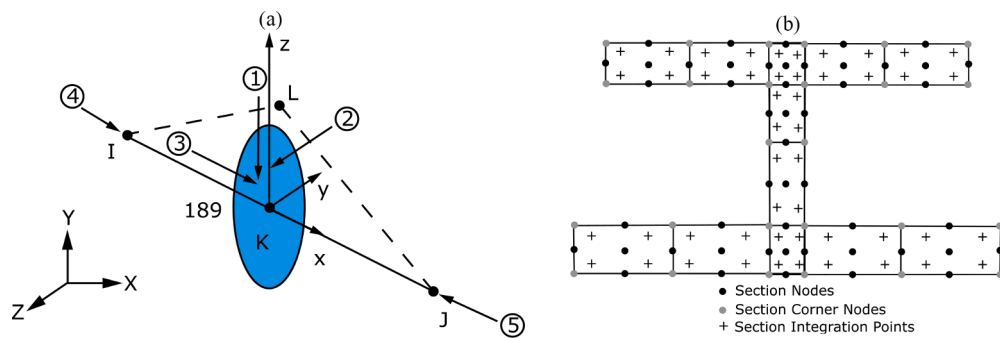

Fig. 8. (a) BEAM189 definition. (b) cells and nodes of the cross-section pseudo-mesh [49].
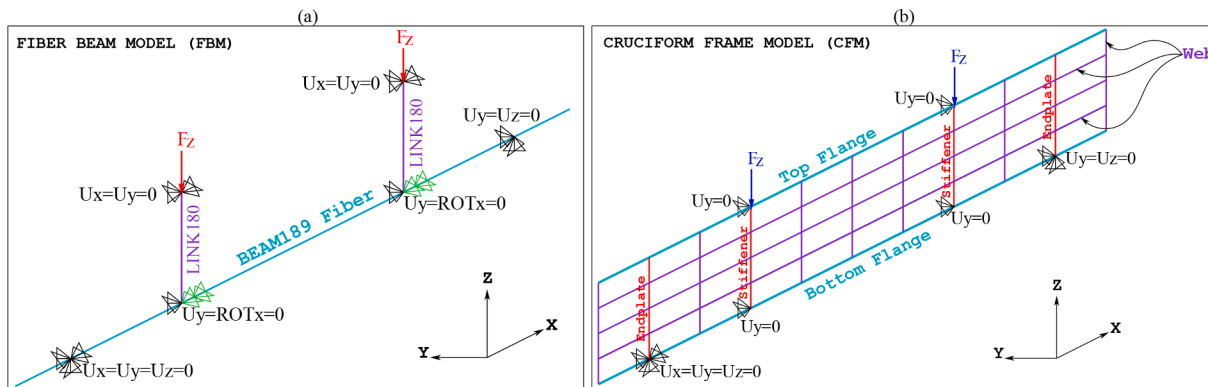

Fig. 9. Idealization of the tested beam in each proposed modeling strategy. (a) FBM. (b) CFM.

2. Eigenvalue analysis (linear elastic buckling analysis).

3. Implementation of initial imperfections.

4. Implementation of internal residual stresses.

5. Application of the first load phase called thermal conditioning, henceforth. This phase includes the progressive heating of the model up to the target temperature level and the activation of self-weight stresses. Additional thermal stresses and strains are generated in this phase.

6. Application of the second load phase called post-conditioning, henceforth. This phase includes the application of loading by increments maintaining the loads from the previous stage.

7. Results of displacements, applied load, ultimate load, and the ultimate moment of the section.

4.1. Finite element model definition

A fiber model (FBM) and a cruciform model (CFM) are created to simulate the LTB of FIDESC4 Test-1 and Test-3 following the idealizations shown in Fig. 9a and b. In the FBM, lateral restraint in the global *y-y* direction and torsional restraints to ensure stability are applied to the two nodes on the fiber axis, matching the location of stiffeners. Lateral restraint in the *y-y* direction and an axial restraint in the *x-x* direction are imposed on the LINK180 end nodes where the stiffeners are located, as shown in Fig. 9a. In CFM, *y*-displacements are null in the four nodes where the imposed lateral restraint is, as shown in Fig. 9b. In both FBM and CFM modeling strategies, displacements in all global axes are restrained in the first point pinned support, and displacements in global *y-y* and *z-z* axes are restrained in the second one. The stress–strain ratio (σ-ε) of steel at high temperatures and the reduction factors $k_{y,\theta}$, $k_{p,\theta}$ and

$k_{E,\theta}$ given by EN 1993-1-2 [16] were used in the models. The values of yield strength and elastic modulus of materials for flanges, web, and stiffeners at room temperature used for modeling were given in Table 1. A constant Poisson ratio ($\nu = 0.3$) was also assumed. The creep effect on the deformation of steel was considered implicit in the material model. The ANSYS multi-lineal isotropic hardening with temperature dependence model was used to adequately represent the stress–strain relationships depending on temperature [52]. Variation of thermal expansion (α) of steel with temperature was also determined based on EN 1993-1-2 [16]. The geometric nonlinearity was activated to introduce the formulations of large deformations and deflections. All numerical model data were taken from the FIDESC4 investigation report [24], and some validation details were taken from Prachar et al. [29,30].

4.2. Eigenvalue analysis

An eigenvalue analysis was carried out to establish the initial imperfections in the numerical models of the tested beams. The buckled mode shapes (global and local) resulting from eigenvalue analysis approximately represent the global and local imperfection shapes measured before the test. The eigenvalue buckling analysis process includes two steps: a linear static solution and an eigenvalue buckling solution. The first step involves a linear analysis with unit loads (Fz = 1 kN in Fig. 9). In the second step, the eigenvalues are calculated, and the elastic buckling analysis is expanded to find the buckling mode shapes associated with each calculated eigenvalue. Two buckling mode shapes are selected adequately after that, i.e., one consistent with the measured global imperfection shape and the other congruent with the local imperfection profile on the web measured in the central part of the beam. According to [24], a simple lateral curvature in the y-y direction characterizes the global buckling mode shape, and the local buckling mode shape resembles well-defined undulations in the y-y direction in the central part of the beam. E.g., six undulations (three peaks and three valleys) on the web for Test-1 and eight undulations for Test-3 [24]. The nodal solution for the global and local buckling modes can be expanded to the pseudo-mesh nodes of the BEAM189 element cross-section in the post-processing stage. In the expansion, vertical undulations also appear in the top flange, which can be evidenced in the extruded view. These web and top flange undulations represent the shape of the initial geometric imperfections measured on the tested beams used in the LTB simulations. The amplitude or absolute maximum value of the imperfections is extracted from the two selected buckling mode shapes in order to scale them to the size of the measured amplitudes. In the proposed strategies, the global amplitude is the maximum lateral deflection, in the y-y direction, of the selected global mode shape. This global amplitude is extracted from the entire model. The local amplitude on the web is the maximum lateral deflection, in the y-y direction, of the selected local mode shape. The local amplitude in the top flange is the maximum vertical deflection, in the z-z direction, of the selected local mode shape. The local amplitudes are extracted from the heated zone (central part) of the beam model because this was the location where the imperfections were measured.

4.3. Implementation of initial imperfections

In order to simulate the initial shape with imperfections, the geometry of the finite element model is updated according to the displacement results of the global and local buckling mode shapes (obtained from the previous eigenvalue analysis) so that a modified geometry based on the deformed configuration of the previous analysis is created. In other words, the displacement results of the global and local buckling mode shapes on the original geometry are added. Before being added together, these displacements are multiplied by a factor that scales and weights them. This factor is responsible for adding a percentage of the displacements to the geometry of the finite element model (e.g., factor 1.0 adds the full value of the displacements to the geometry of the finite

element model). This factor results from multiplying two other factors, i. e., one for scaling and one for weighting. The scale factor is a multiplier that adjusts the displacements of each buckling mode shape to the size of the measured imperfection amplitude. The scaling factor is determined as the ratio of the measured imperfection amplitude (given in Table 2) to the simulated amplitude. Therefore, three scaling factors are defined, one to scale the y-y displacements of the global mode shape, and two for scaling the y-y and z-z displacements of the local mode shape. These simulated amplitudes are extracted after the local and global buckling mode shapes are carefully chosen. The simulated global amplitude in the y-y axis is extracted from the entire model, while the simulated local amplitudes (on the web about the y-y axis and the top flange about the z-z axis) are drawn from the central part of the beam. GSF is the global scale factor, and LSF1 and LSF2 are the local scaling factors on the web and top flange, respectively. They are calculated following Eqs. (1)–(3).

$$GSF = \frac{\text{Measured global imperfection amplitude}}{\text{Simulated global amplitude}(y-y \text{ axis})} \quad (1)$$

$$LSF1 = \frac{\text{Measured web local imperfection amplitude}}{\text{Simulated local amplitude } (y-y \text{ axis})} \quad (2)$$

$$LSF2 = \frac{\text{Measured top flange local imperfection amplitude}}{\text{Simulated local amplitude}(z-z \text{ axis})} \quad (3)$$

The participation factor is responsible for weighting the displacements of each buckling mode shape (global and local). It defines the portion of the displacements of each two buckling mode shapes contributing to the initial imperfect geometry. GPF denotes the participation factor of the global mode shape displacements and, LPF1 and LPF2 are the participation factors of the web and top flange displacements of the local mode shape, respectively. In the proposed numerical modeling strategies, each participation factor is assumed to be 1/3 due to the number of imperfection amplitudes measured, as shown in Eq. (4).

$$GPF = LPF1 = LPF2 = 1/3 \quad (4)$$

In this way, the imperfections added to the original geometry are the scaled and weighted displacements of the global and local buckling mode shapes. The nodal x, y, z-displacement results of global and local mode shapes are stored in arrays denoted as GMS and LMS, respectively. Therefore, GMS contains the nodal displacements of the global mode shape, and LMS contains those of the local mode shape in the central zone of the beam. Thus, the imperfections added by the global mode shape (called GI) and those added by the local mode shape (called LI) result from scaling and weighting the GMS and LMS arrays with the scaling and participation factors, as shown in Eqs. (5) and (6). Therefore, GI and LI can be understood as arrays of nodal imperfections (equivalent to the scaled and weighted nodal displacements). GI stores the imperfections of each node of the finite element model, while LI stores the node imperfections in the central zone of the beam model.

$$GI = \underbrace{GMS(GSF \times GPF)}_{\text{Whole beam}} \quad (5)$$

$$LI = LMS(\underbrace{\overbrace{\underbrace{LSF1 \times LPF1}_{\text{Web}} + \underbrace{LSF2 \times LPF2}_{\text{Top Flange}}}^{\text{Central zone}}}) \quad (6)$$

However, in the FBM and CFM modeling strategies, the scaling factor over the local imperfection of the top flange (LSF2) cannot be considered in Eq. (6). That is because the simulated local imperfection amplitude in the z-z direction is on the fiber axis and not in the cross-section of the elements, so this amplitude cannot properly represent the maximum simulated imperfection at the top flange edges where the local imperfections were measured. Nevertheless, it was considered that the imperfections on the top flange could be approximately included through the local cumulative participation factor (LCPF) of 2/3, as shown in Eq.

(7), which compensates for the non-inclusion of the local top flange imperfection. In other words, the local mode shape contribution was increased by 1/3. Therefore, the local imperfection array (LI) results from scaling the nodal displacements (in the *x*, *y*, *z*-directions) of the local mode shape with the scaling factor LSF1 and weighting them with the local cumulative participation factor LCPF, as shown in Eq. (8).

$$LCPF = LPF1 + LPF2 = 2/3 \qquad (7)$$

$$LI = \underbrace{LMS(LSF1 \times LCPF)}_{Web\ (Central\ zone)} \qquad (8)$$

To approximate the imperfect initial geometry (IIG) of the model, first, the global imperfections (GI) are added to the node coordinates of the finite element model. Then, from this revised geometry, local imperfections (LI, in Eq. (8)) are added to the node coordinates of the central zone of the beam model, as illustrated in Eq. (9). The node coordinate array of the model is denoted in Eq. (9) as FGC (Full Geometry Coordinates), and that of the beam central zone is denoted as CGC (Central Geometry Coordinates). The largest displacements of the global and local buckling mode shapes are in the *y-y* direction, and displacements in the two other directions are too small (10E-13) so that the small displacements after scaling and weighting remain so. Therefore, *x-x* and *z-z* imperfections added to *x* , *z*-coordinates are too minor, so this methodology to create imperfections is correct.

$$IIG = \underbrace{[FGC + GI]}_{Whole\ beam} + \underbrace{[CGC + LI]}_{Central\ zone} \qquad (9)$$

The web resulting shape in the central zone of the beam is a combination of the global and local imperfections. Out of the central part of the beam, only global imperfections are present. After that, the resulting imperfect shape is expanded to the cross-section pseudo-mesh nodes of the BEAM189 elements in the post-processing. As a result of the expansion, undulations appear out of the beam axis on the top flange edges. The resulting undulations on the web and the top flange after expansion depict the initial imperfections of the model.

4.4. Implementation of residual stresses

According to how the test was carried out, initial axial residual stresses are incorporated into the proposed numerical models of the tested beams before applying thermal and mechanical loadings. Residual stresses at room temperature are relevant because they act as an initial stress condition (σ_{x0}). In the finite element formulation of the problem, initial stresses and initial strains (ε^o) represent elementary equivalent nodal forces in the equilibrium equations. Therefore, they are part of the total equivalent nodal forces integrated by other force components such as body and surface forces and forces produced by initial strains coming from the thermal action [53]. In summary, the residual stresses are part of the global equilibrium of the finite element mesh and the stress field of the structure, so they must be considered.

BEAM189 finite elements allow the application of these axial residual stresses in the cross-section pseudo-mesh cells. The cells are set so that the tensile and compressive residual stresses in the web and flanges can be applied as closely as possible over the cross-section regions where they are localized. Fig. 10 presents the residual stress pattern at room temperature for the welded I-section considered by FIDESC4 [24] based on [54], used in this study. In Fig. 10, the residual stresses act in the whole cross-section. The yield stress values f_y are at room temperature, and red areas (T) represent tensile stress while blue areas (C) represent compressive stress.

4.5. Application of the thermal conditioning

In the experiments, progressive heating of the central zone of the beam is performed from 20 °C until the target temperature level at each
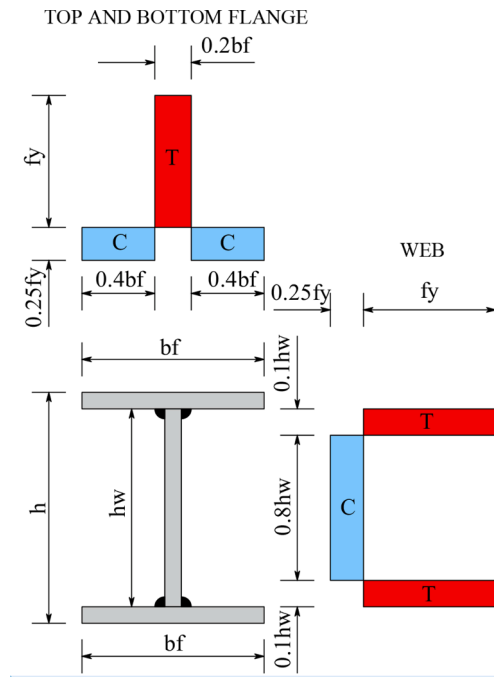

Fig. 10. Residual stress pattern for welded I-section at room temperature. Above: for both top and bottom flanges. Right: Web [24,54].

part (top flange, web, and bottom flange) is attained before applying the mechanical load (thermal conditioning). This change in the temperature results in thermal strains (ε_x^o) [55]. The non-uniform temperature in the cross-section causes initial bending resulting in thermal stresses (σ_x^o) that combine with initial residual stresses (σ_{x0}) and self-weight stresses (σ_x) modifying the initial stress state. Moreover, the Poisson effect induces transverse thermal strains ($\varepsilon_y^o, \varepsilon_z^o$) in the central zone of the beam that intensifies the initial geometric imperfections; in consequence, a revised imperfect geometry is generated. Furthermore, the temperature degrades the material and changes the stiffness in the central zone. As the side spans are unheated, their stiffness is higher than the stiffness of the central zone, acting as semi-rigid boundaries over the middle span (see Fig. 11), causing some *y*-rotation restraints in these frontiers. Additionally, lateral stresses (σ_y^o) are induced on the stiffener ends (red points in Fig. 11) due to the lateral restriction imposed by the frameworks. As a result, axial and vertical strains ($\varepsilon_x^o, \varepsilon_z^o$) are generated by the Poisson effect. In summary, the thermal conditioning modifies the initial state of the tested beams, among others, for the following reasons: 1) the appearance of a thermal stress–strain state caused by the temperature rise from 20 °C to the target temperature in each part of the beam and bending due to non-uniform temperature distribution in the cross-section, 2) the Poisson effect, 3) the appearance of additional imperfections, 4) the formation of semi-rigid boundaries. It should be noted that the geometric imperfections are the result of thermal strains. The initial geometric imperfections come from the thermal strains produced in the manufacturing and cutting process of the plates. In the thermal conditioning stage of the tested beams, the additional geometric imperfections come from the thermal strains produced by the temperature increase and the temperature differential of the cross-section. Finally, thermal strains must be activated in the simulation of the tested beams to account for all the effects of high temperatures in the thermal conditioning stage.

According to how the test was carried out, the thermal condition is included in the numerical models of the tested beams before applying mechanical loadings. To do so, ramped temperature for a time t = 1E−08 min is applied starting from the room temperature (20 °C) up to the target temperature at each part (top flange, bottom flange, and the
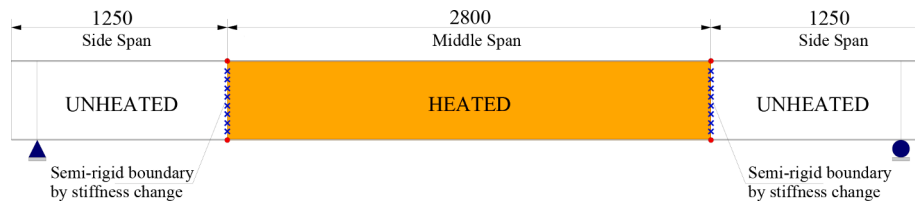
Fig. 11. Semi-rigid boundaries produced by stiffness change.

web) shown in Fig. 7a in which non-heated zones are assumed to have a room temperature of 20 °C. The time is arbitrarily chosen as a very small value close to zero because the analysis is static; therefore, the mechanical response in this stage is not dependent on time. Once the residual stresses, temperature from thermal conditioning, and self-weight loads are applied, a first GMNIA is done here. Results of deformed shape (perturbed shape) and all analysis results are the starting point for the second GMNIA carried out in the next phase, including the controlled displacement mechanical loading.

4.6. Application of post-conditioning

According to how the test was performed, this second loading phase starts from the deformed shape and the stress–strain results of the previous analysis. In this second phase, the self-weight and the temperatures in each part of the beam (flanges, web, and stiffeners) remain applied. Additionally, the vertical load is applied to the upper nodes of the stiffeners through the displacement-controlled method at a rate of 3.5 mm/min during 6.5 min. Therefore, Fz (see Fig. 9) is applied as a vertical displacement (Uz) until a target value of 22.75 mm. This target
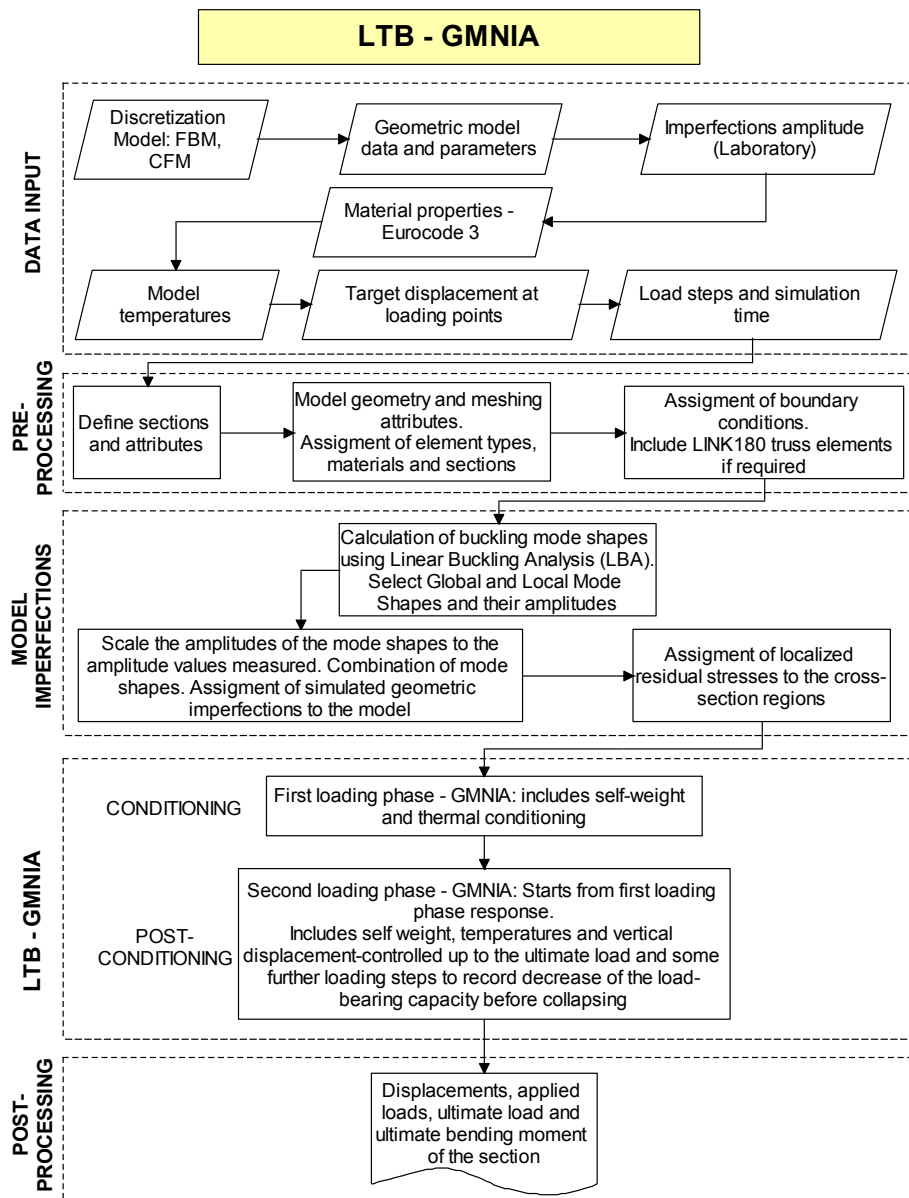

Fig. 12. Full LTB-GMNIA for the FIDESC4 tested beams.

displacement value is enough to evidence the load behavior, including the ultimate load and the load-bearing capacity decrease of Test-1 and Test-3. In the FIDESC4 simulations [24], the load capacity was registered up to 25 mm of mid-span vertical deflection for Test-1 and 30 mm for Test-3. Once loads in this phase are applied, the full GMNIA-LTB is done.

4.7. Results

At the end of the GMNIA, time history results of the top flange vertical mid-span displacements, the applied load, ultimate load, and ultimate bending moment are obtained. The full GMNIA procedure implemented in the proposed numerical modeling strategies (FBM and CFM) is illustrated in Fig. 12.

5. Implementation of ltb-gmnia in the proposed modeling strategies

Hereafter the implementation of the LTB-GMNIA in the proposed FBM and CFM modeling strategies is explained in detail for Test-1. The reason is that the methodology of each strategy is the same for the tested FIDESC4 beams whit constant cross-section.

5.1. Fiber beam model (FBM)

The tested beam subjected to LTB is idealized as a single fiber of 342 BEAM189 finite elements with endplates and stiffeners included. In this model, each finite element has a cross-section and a material depending on the part of the beam it represents, e.g., web, flange, endplate, or stiffener. The beam is made of three distinct types of cross-sections (welded I-section, endplate, and stiffener) and three different types of materials (one for endplates and stiffeners, and two materials for flanges and web -S2 and S5, respectively as shown in Fig. 2a and Table 1). Therefore, three different sections and three different materials are defined in the model. Cross-sections are assigned to finite elements, while materials are assigned to the pseudo-mesh cells of the cross-section. This way to assign materials by cells enables differentiating zones with different materials in the steel member, i.e., flanges and web materials, and endplate and stiffener materials. The number of cells in the cross-section is set to apply the residual stress pattern shown in Fig. 10. For this purpose, 75 cells were defined at each flange and 50 cells at the web, as shown in Fig. 13.

The fiber axis is moved to the outer edge of the bottom flange, where the boundary conditions are applied, which means boundary conditions are eccentric. LINK180 truss elements between the two flanges transfer the load from the application points on the outer surface of the top flange to the outer surface of the bottom flange, where the fiber axis is located. Thus, LINK180 elements have the cross-section area of the stiffeners given in Fig. 2a. The meshing and boundary conditions in the fiber are shown in Fig. 14a, and the tested beam extruded in which all its components are visible is shown in Fig. 14b.

Figs. 15 and 16 show the global and local buckling mode shapes chosen from the eigenvalue analysis. In the extruded view of Fig. 15b, a simple lateral curvature in the y-y direction is clearly observed. In the local mode shape of Fig. 16b, the slight lateral undulations in the central part of the beam depict the local imperfections on the web. Although this is a single fiber model, the extruded local shape in Fig. 16b also shows undulations on the top flange, allowing for the simulation of the measured local imperfections. Undulations out of the central part of the beam in Fig. 16b are not considered because local imperfections are only applied to the central zone of the beam where they were measured. In the FBM, it is assumed that the displacements in the y-y direction are from the web. Therefore, the simulated amplitude in the y-y direction is the maximum lateral deflection obtained from the fiber nodes for the global buckling mode shape (in Fig. 15a) and from the nodes in the central part of the fiber for the local buckling mode shape (in Fig. 16a).
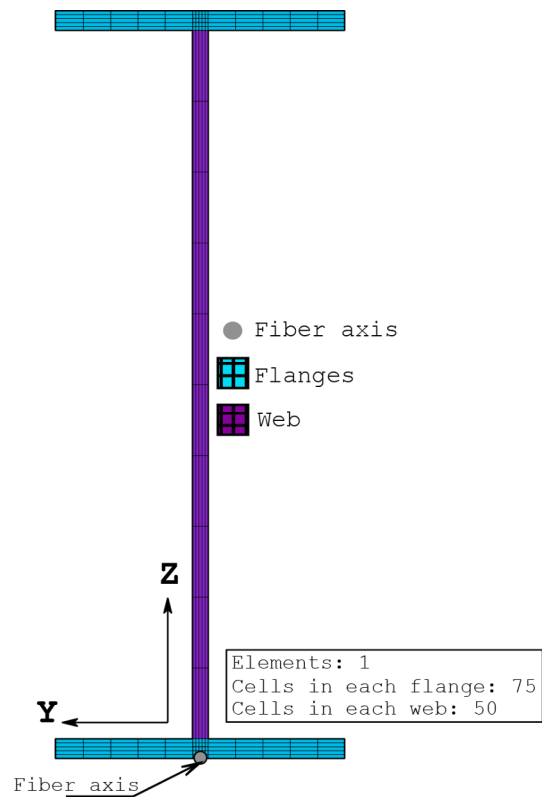

Fig. 13. I-cross-section discretization and cells for Test-1.

The imperfect initial geometry is obtained by adding the imperfections to the node coordinates of the original model, according to Eq. (9). In both global and local mode shapes, x-displacements and z-displacements are almost zero on the fiber axis, so that x-imperfections and z-imperfections adding to x-coordinates and z-coordinates of the FBM are also almost null. Consequently, the x-coordinates and z-coordinates of the FBM are practically identical in the original and imperfect geometry. As y-coordinates, in this case, are zero, the imperfections in the y-y direction are equal to the y-coordinates of the FBM imperfect initial geometry. Since, in the FBM, the beam is modeled as a single BEAM189 finite elements fiber, it is assumed that the displacements in the y-y direction are from the web. Therefore, the y-y amplitude of the global and local mode shapes is used for calculating the global and local scale factor, GSF and LSF1, as shown in Eq. (1) and Eq. (2). Also, the global and local displacements occurring in the lateral direction are used to calculate the global and local y-imperfections, according to Eq. (5) and Eq. (8). The FBM y-y imperfections are plotted in Fig. 17. These are obtained from combining the scaled and weighted lateral displacements of both buckling mode shapes and are located in the central zone of the beam, as expected. The null imperfections in Fig. 17 match the points of the stiffeners and endplates where the y-displacement boundary condition is restrained in the model. Out of the central zone of the beam, very small imperfections are coming from global y-displacements.

According to Fig. 10, compressive (blue) and tensile (red) axial residual stresses at room temperature in the web and flanges are applied to the cross-section pseudo-mesh cells of the BEAM189 element, as shown in Fig. 18.

BEAM189 finite elements making up the fiber do not have temperature degrees of freedom. However, they support uniform temperature loading and linearly varying thermal gradients within the cross-section [49]. These two components allow representing the non-uniform transverse temperature distribution in the element. For this reason, in the thermal conditioning stage of the LTB-GMNIA (see Fig. 12), the target temperature is established by a uniform temperature and a
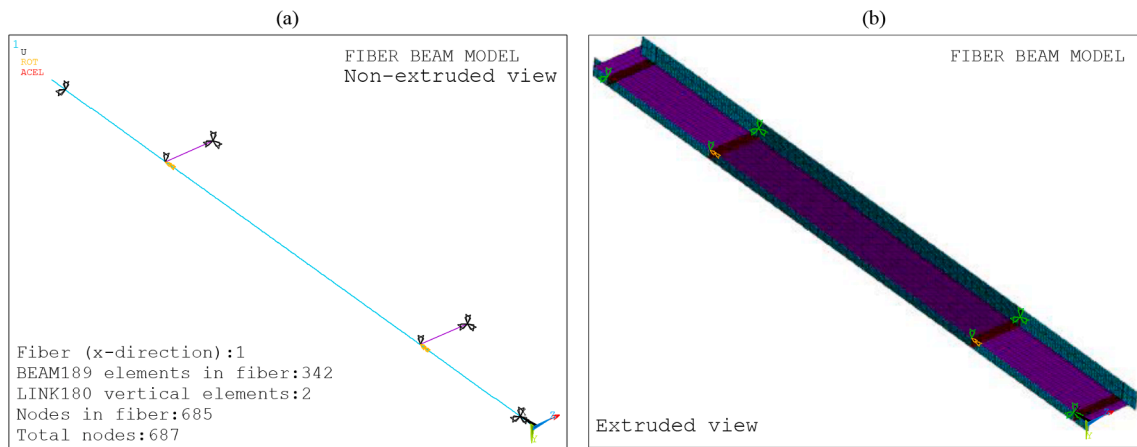
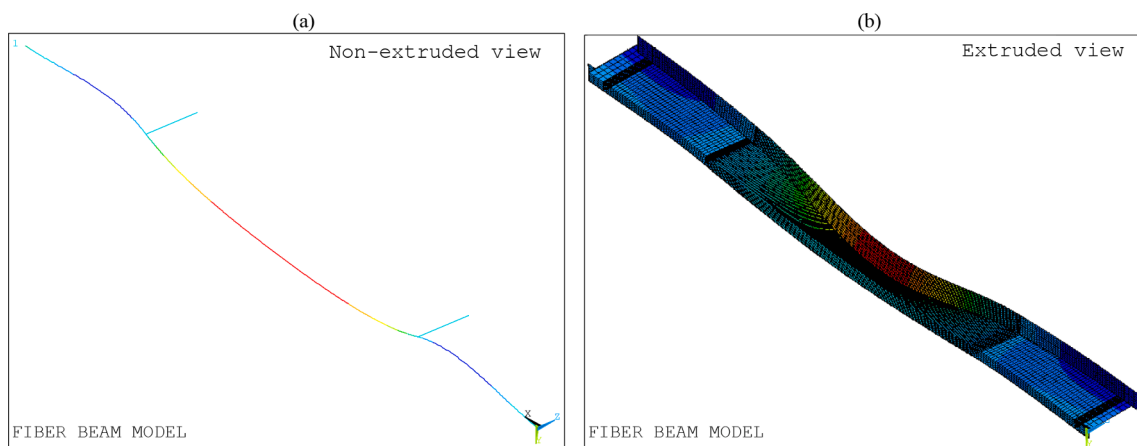**Fig. 14.** FBM meshing and boundary conditions for Test-1. (a) Non-extruded view. (b) Extruded view.

Fig. 15. FBM global mode shape for Test-1. (a) Non-extruded view. (b) Extruded view.
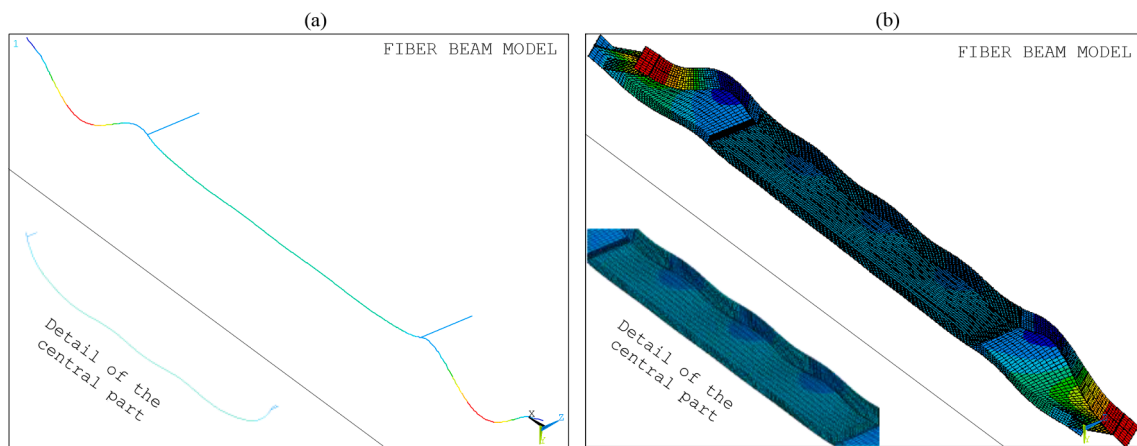

Fig. 16. FBM local mode shape for Test-1. (a) Non-extruded view. (b) Extruded view.

vertical gradient (in *z-z* axis) [38] to be attained in the BEAM189 elements in the central part of the beam following the procedure described in the thermal conditioning phase. Additionally, a target uniform temperature equal to that of the web in the test (444.4 °C) is specified in the BEAM189 elements symbolizing the stiffeners and LINK180 elements representing the load axes.

The two components approximating the non-uniform temperature in the cross-section are calculated by linear regression from the temperatures measured in the web and flanges (shown in Fig. 7a), as illustrated in Fig. 19.

In this sense, the non-uniform temperature in the cross-section (Fig. 20a) is approximated by two components:

– A uniform temperature component (Fig. 20b) equal to the linear regression intercept (367.02 °C in Fig. 19).
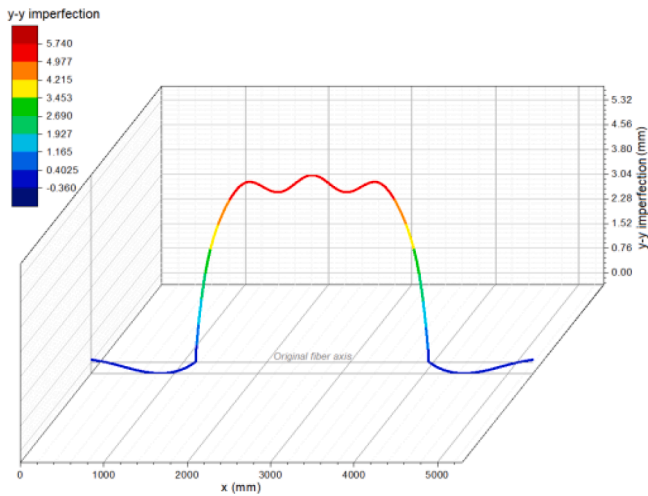
Fig. 17. Imperfect initial geometry of FBM for Test-1 (mm).

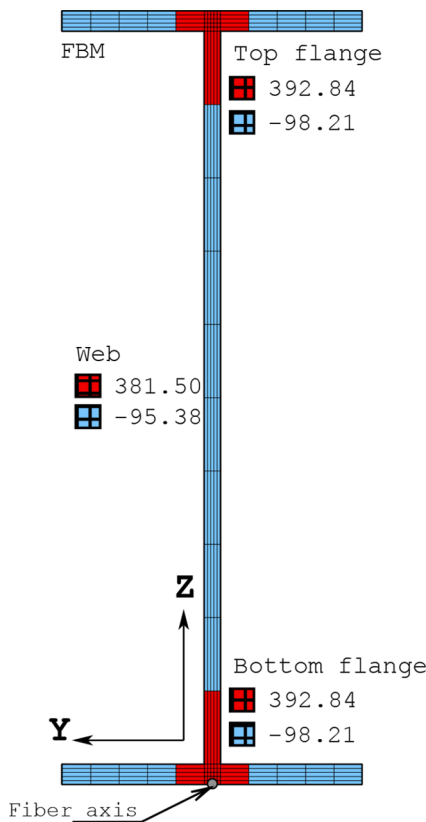**Fig. 19.** Approximation of non-uniform temperature in the BEAM189 cross-section (Test-1).

Fig. 18. FBM tensile and compressive residual stresses in the welded I-section for Test-1 [MPa]

– A component of thermal gradient varying linearly on the *z-z* axis (Fig. 20c) equal to the slope of the regression line (0.23 °C/mm in Fig. 19).

The uniform temperature component is applied at the lowest point of the BEAM189 cross-section since the fiber axis is at the outer edge of the bottom flange. So, the temperature at one point of the cross-section is approximated by Eq. (11).

$$Temp(z) \approx Unif\ Temp + Temp\ Grad(z) \times Z \tag{11}$$

In Eq. (11), *Unif. Temp* is the approximate temperature value at the

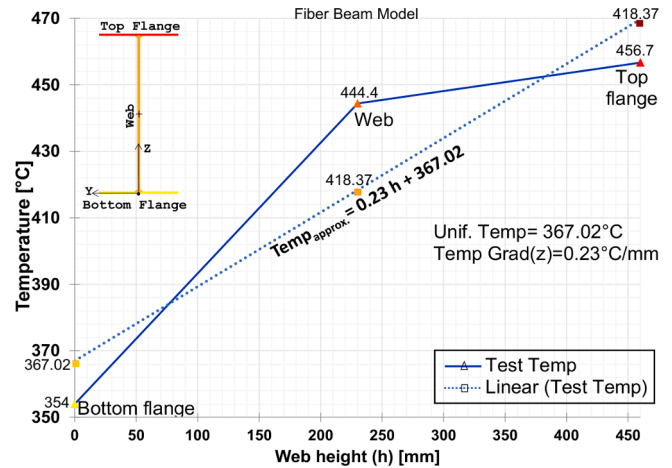bottom flange (367.02 °C), *Temp Grad(z)* is the thermal gradient in the web direction (0.23 °C/mm), and Z is the coordinate of a section point. Z-coordinates are positive since the reference system origin is at the outer point of the section over the fiber axis. As the gradient line passes through the lowest point of the cross-section, the gradient component is null at that point. Consequently, the temperature applied at the lowest point of the section is equal to the uniform temperature.

In the post-conditioning stage, the vertical load is applied at the upper-end nodes of the LINK180 elements by incremental displacements until the target value of 22.75 mm is attained. This target displacement value is adequate to record the ultimate load and the load-bearing capacity drop. A uniform temperature and a *z-z* gradient are instantaneously applied to BEAM189 elements in the central part of the beam in this phase. The web temperature (444.4 °C) is also instantly applied as a uniform temperature in the BEAM189 elements representing the stiffeners and LINK180 elements. Fig. 21 shows a detail of the extruded stiffener displaying the controlled-displacement boundary condition. Time histories of vertical deflection (Uz) at the midpoint of the fiber and the force (Fz) in the top-end node of LINK180 elements are obtained at the end of the GMNIA.

5.2. Cruciform Frame model (CFM)

In the CFM, the tested beam subjected to LTB is idealized as a cruciform arrangement of fibers, where each fiber is made up of BEAM189 elements with rectangular cross-sections. This grid arrangement enables considering two bending directions for the web and better predicts the localized buckling produced by the high compressions on the thin web plate. The discretization consists of a grid of BEAM189 elements representing the web (illustrated in Fig. 22a in purple). Above and below the grid are grid lines idealizing the top and the bottom flange (cyan colored in Fig. 22a). The number of grid divisions in the vertical direction (*ndv*) is taken as 10, and the number of grid divisions in the longitudinal direction (*ndl*) is taken as 106. Therefore, the web is modeled with a grid with 11 horizontal fibers and 107 vertical fibers. In total, the web is made up of 1166 horizontal elements and 1070 vertical elements cruciform arranged. In turn, each flange is a fiber of 106 finite elements. Endplates and stiffeners are also vertical fibers of BEAM189 elements (red-colored in Fig. 22a), and they have the material and the cross-section indicated in the test (see Fig. 2a and Table 1). The cross-section dimensions of the flange elements are the width and thickness of the thin plate defining the flanges (150.0 × 5.0 mm, in Fig. 3a). Besides, the material of the flange elements is that of the test (S5, in Fig. 2a). The cross-section dimensions of the web elements are 45.5 × 4.0 mm for the horizontal elements and 50.0 × 4.0 mm for vertical
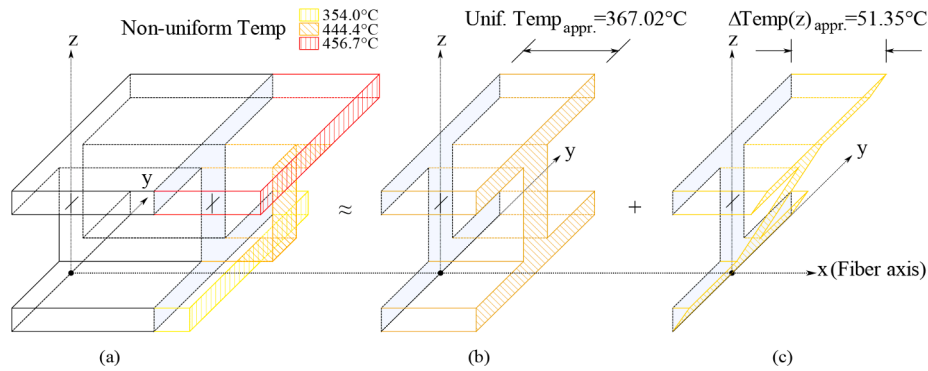
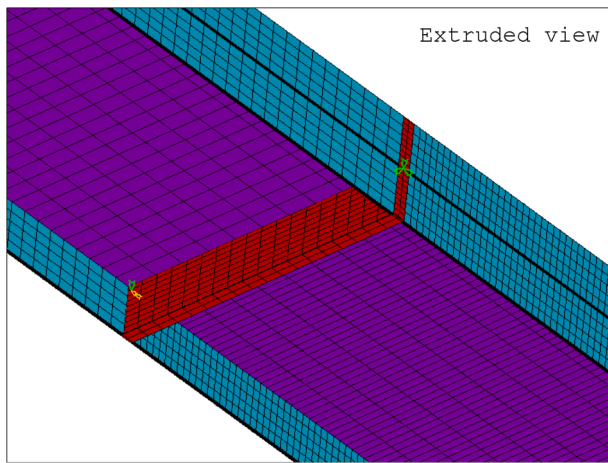**Fig. 20.** Temperature components related to BEAM189 element axes (Test-1).

Fig. 21. FBM stiffener detail for Test-1.

elements (4.0 mm is the thickness of the web plate, in Fig. 3a). The material of the web elements is the same as the web plate in the test (S2, in Fig. 2a). Lateral restraints in the global *y-y* direction are applied to the two nodes of the upper fiber where the load is applied and the two nodes of the lower fiber where the stiffeners are. Fig. 22b shows the finite element mesh extruded, showing all the components and the boundary conditions. Fig. 23 shows one vertical and one horizontal web fiber and the dimensions of their constituent BEAM189 elements.

The welded I-section is represented by the rectangular cross-sections of all its component elements, as shown in Fig. 24. The cross-sections of horizontal grid elements constitute the web. Each I-section flange is the

cross-section of a BEAM189 finite element in the upper or lower fiber as appropriate. The number of cells in the cross-section of elements forming the welded I-section is set to apply the pattern of residual stresses.

Figs. 25 and 26 show the global and local buckling mode shapes chosen from the eigenvalue analysis, respectively. In Fig. 25b, the simple lateral curvature in the *y-y* direction typical of the global mode shape can be appreciated. In the local mode shape of Fig. 26a, the lateral undulations allow depicting the local web imperfections. Vertical undulations in the top flange in the extruded view of Fig. 26b are not visible in the non-extruded view of Fig. 26a. This occurs because, in the non-extruded deformed shape, only the fiber axes are shown. It means the fiber axis representing the top flange is not deformed, but its edges do, as expected. In the central zone of the beam, the extruded deformed shape of the top flange resembles a saddle surface containing various saddle points. The undulations of this surface depict local imperfections on the top flange. In the CFM, it is assumed that the displacements in the *y-y* direction are from the web. Therefore, the simulated amplitude in the *y-y* direction is the maximum lateral deflection obtained from the grid nodes for the global mode shape (in Fig. 25) and the grid nodes of the central part of the grid for the local buckling mode shape (in Fig. 26).

The imperfect initial geometry is obtained by adding the imperfections to the node coordinates of the original finite element model, according to Eq. (9). In both local and global mode shapes, *x*-displacements and *z*-displacements are almost zero on the CFM fiber axes, so that *x*-imperfections and *z*-imperfections adding to *x*-coordinates and *z*-coordinates of the CFM are neglected. Consequently, the *x*-coordinates and *z*-coordinates are practically identical in the original geometry and the imperfect geometry. In the *y-y* direction, the imperfections are non-zero, but the *y*-coordinates of the original model, in this case, are zero. Therefore, the *y-y* imperfections are equal to the *y*-coordinates of the initial imperfect geometry. The global and local scale
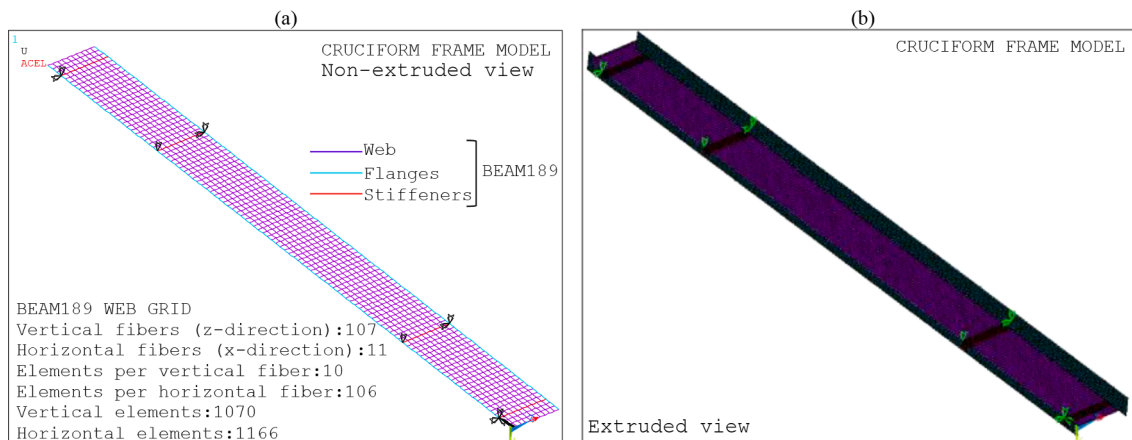

Fig. 22. CFM meshing and boundary conditions for Test-1. (a) Non-extruded view. (b) Extruded view.
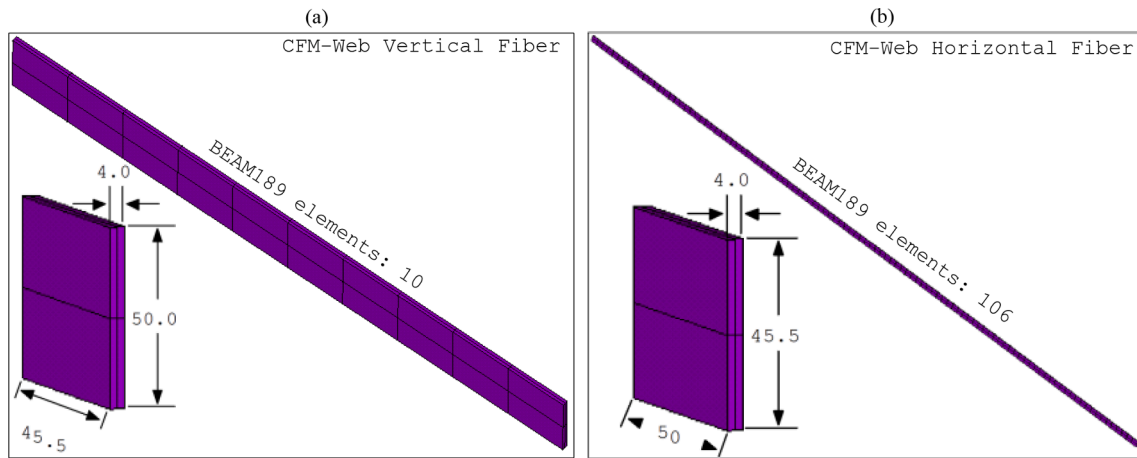
Fig. 23. Details of the CFM web fibers and dimensions of the fiber elements for Test-1, in mm. (a) Vertical fiber. (b) Horizontal fiber.
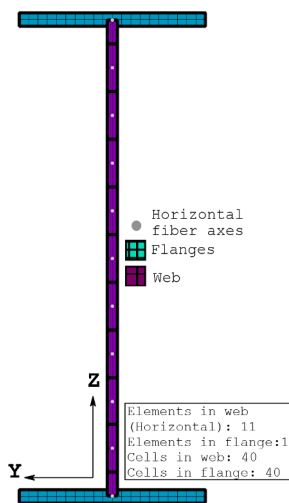

Fig. 24. CFM cross-section discretization and element cells for Test-1.

factors, GSF and LSF1, are calculated according to Eqs. (1) and (2), and the global and local *y*-imperfections are calculated as shown in Eqs. (5) and (8). The *y-y* imperfections plotted in Fig. 27 show similar positive and negative values. The imperfection values are obtained from combining the scaled and weighted lateral displacements of both buckling modal shapes and are present in the central zone of the beam,

as expected. Out of the central zone of the beam and in the flanges, the *y-y* imperfections are null.

Compressive (blue) and tensile (red) residual stresses at room temperature in the web and flanges are applied to the cross-section cells of the BEAM189 elements that comprise the welded I-section, as shown in Fig. 28.

For the thermal conditioning stage of the LTB-GMNIA, the target temperature at each part (top flange, bottom flange, and web) in the central zone of the beam (show in Fig. 7a) is directly specified as a uniform temperature to be attained in the BEAM189 elements of the top and bottom fibers (flanges) and the grid elements (web). Additionally, the web temperature (444.4 °C) is directly specified as a uniform temperature to be attained in the BEAM189 elements representing the stiffeners. In the post-conditioning stage, the vertical load is applied at the top ends of the stiffeners by incremental displacements until the target value of 22.75 mm is attained. Uniform temperatures measured at each part of the beam are again applied instantaneously in this phase. Fig. 29 shows a detail of the extruded stiffener with the controlled-displacement boundary condition indicated. Time histories of vertical deflection (*Uz*) at the mid-point of the grid lower fiber and the force (*Fz*) in the top-end node of BEAM189 stiffeners are obtained at the end of the GMNIA.

The summary of the full LTB-GMNIA implemented in both proposed ANSYS modeling strategies for Test-1 and Test-3 is shown in the charts of Fig. 30a and b. The procedures are compatible with beams of constant cross-section.
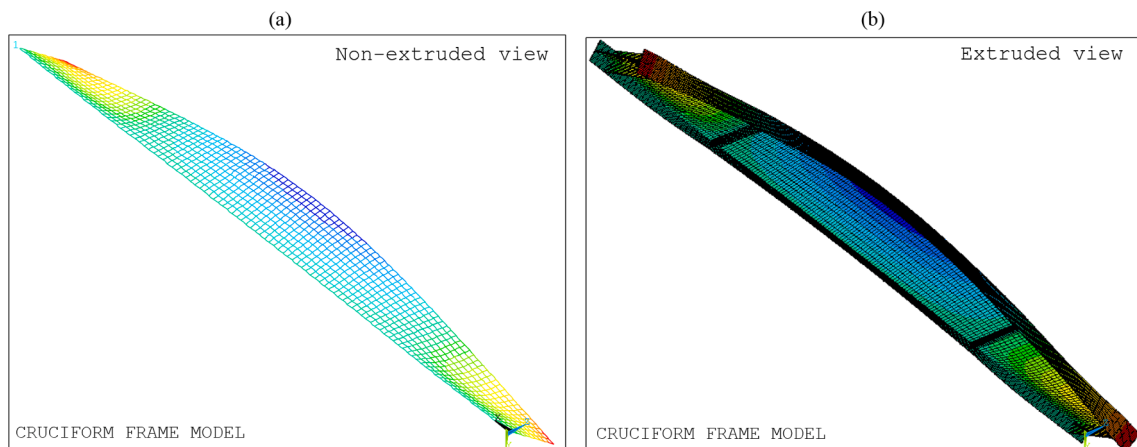

Fig. 25. CFM global mode shape for Test-1. (a) Non-extruded view. (b) Extruded view.
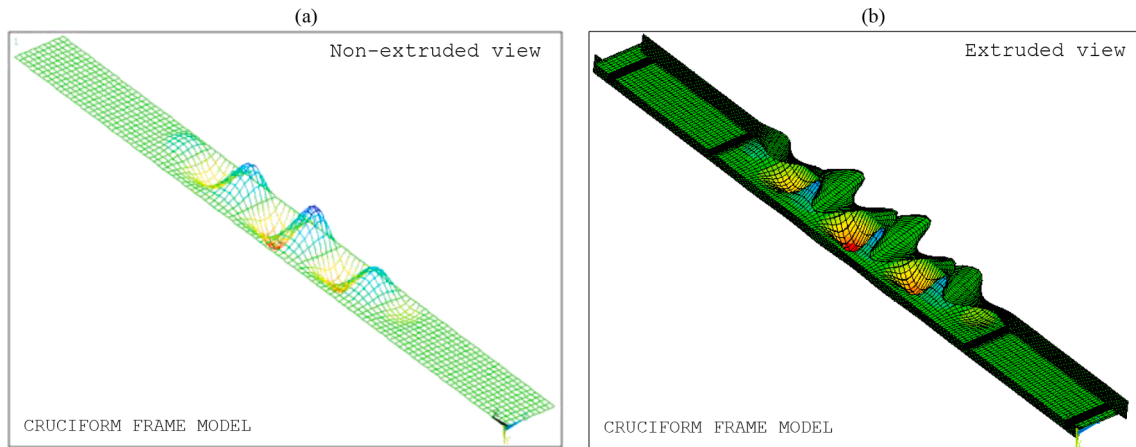
Fig. 26. CFM local mode shape for Test-1. (a) Non-extruded view. (b) Extruded view.
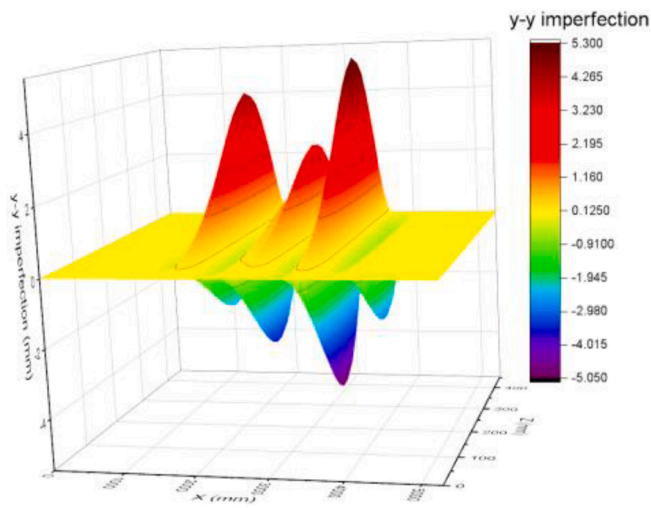

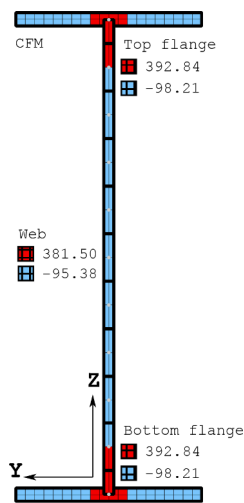Fig. 27. Imperfect initial geometry of CFM for Test-1 (mm).

Fig. 28. CFM tensile and compressive residual stresses in the I-section for Test-1 [MPa]
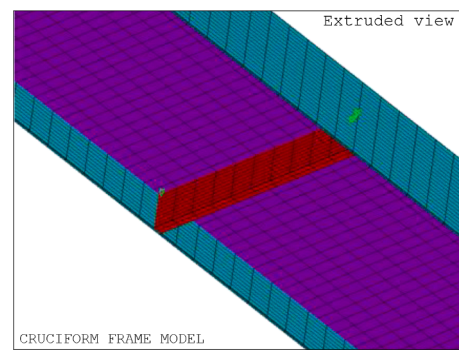

Fig. 29. CFM stiffener detail for Test-1.

5.3. Shell models for numerical validation

Simulations of the tested FIDESC4 beams do not include residual stresses and thermal strains [24,29,30]. Therefore, they do not consider the same conditions as the FBM and CFM, making it challenging to compare numerical results directly. Consequently, new models with ANSYS SHELL181 finite elements for Test-1 and Test-3, called Shell Models (SM, hereafter), were built to compare computation times. SHELL181 is a linear element with four nodes and six degrees of freedom at each node: three translations (Ux, Uy, Uz), and three rotations about the *x, y, z-global* directions (ROTx, ROTy, ROTz). This finite element is suitable in non-linear analyses of large rotations and large deformations where the thickness of the plates can change. It follows the first-order shear deformation theory of Reissner-Mindlin. A brief explanation of the LTB-GMNIA procedure implemented in a shell model is presented only for Test-1 because the methodology is the same for Test-3.

The shell model for Test-1 is based on a geometry of 79 areas shown in Fig. 31a. The discretization is carried out with 14,596 SHELL181 finite elements following the area distribution of Fig. 31a. The areas of the geometric model match the areas where the residual stresses are present, allowing their application to the shell elements following the tensile and compressive stress pattern of Fig. 10. According to the test setup, displacements in the global *y-y* axis are restrained at the eight points where the lateral restraint was applied (see Fig. 7b). The load is applied at the edges where internal stiffeners are located. Finally, the boundary conditions of the tested beam are imposed and shown in Fig. 31b together with the model mesh.

Fig. 32 shows the global and local mode shapes chosen from the linear buckling analysis. It can be seen that the global and local mode shapes exactly match those of the CFM modeling strategy shown in Figs. 25 and 26. For the global mode shape, the amplitude in the *y-y*
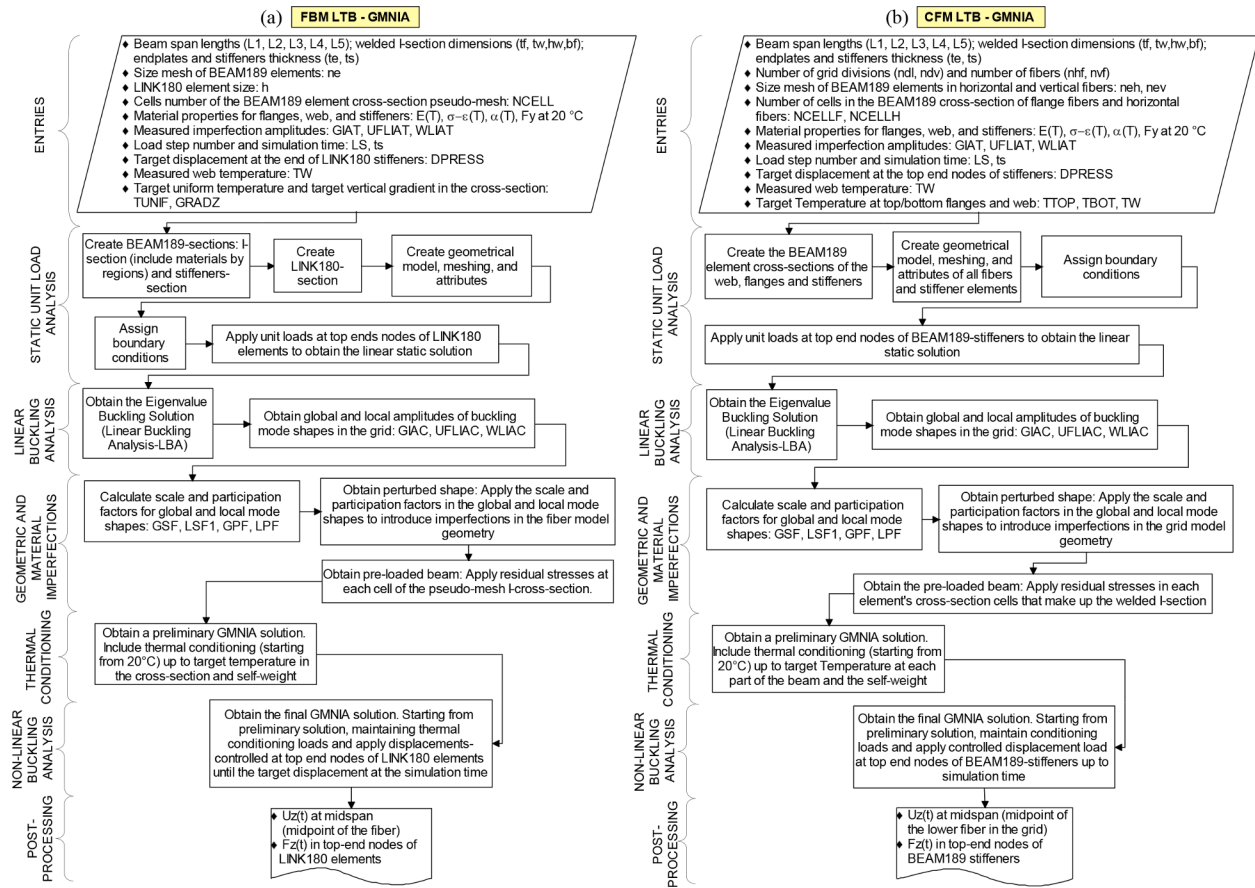
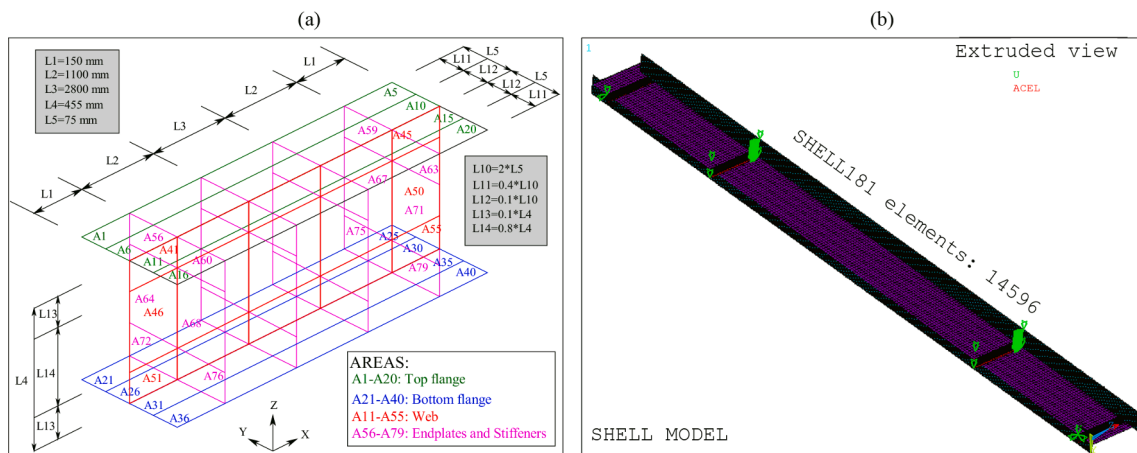**Fig. 30.** Full LTB-GMNIA flowchart. (a) FBM. (b) CFM.

Fig. 31. ANSYS-SM for Test-1. (a) Geometrical model: division into areas. (b) Meshing and boundary conditions.

direction is the maximum lateral deflection calculated at all nodes. For the local mode shape, the amplitudes are extracted from the nodes of the central part of the beam. Thus, the *y*-amplitude on the web is the maximum lateral deflection calculated at web nodes, and the *z*-amplitude on the top flange is the maximum vertical deflection calculated at top flange nodes.

The SM discretization allows the scaling and combination of the two selected buckling modes considering the amplitudes of the measured and calculated imperfections in each beam region. Thus, the scaling factors (GSF, LSF1, and LSF2) are calculated by Eq. (1) to Eq. (3). In this model, the global and local buckling mode shapes contribute in half to

the initial imperfect geometry of the web, meaning the participation factors GPF and LPF1 taking values of ½. On the other hand, the contribution of the local buckling mode shape to the initial imperfect geometry of the top flange is full, meaning the local participation factor LPF2 is 1. Therefore, the global and local imperfections (GI and LI) are estimated according to Eqs. (5) and (6), respectively. Finally, the imperfect initial geometry (IIG) can be approximated by adding the imperfections to the node coordinates of the original model, according to Eq. (9). The web and top flange imperfections are plotted in Fig. 33a and b, respectively. After revising the geometry, these imperfections are obtained by combining the scaled and weighted displacements of the
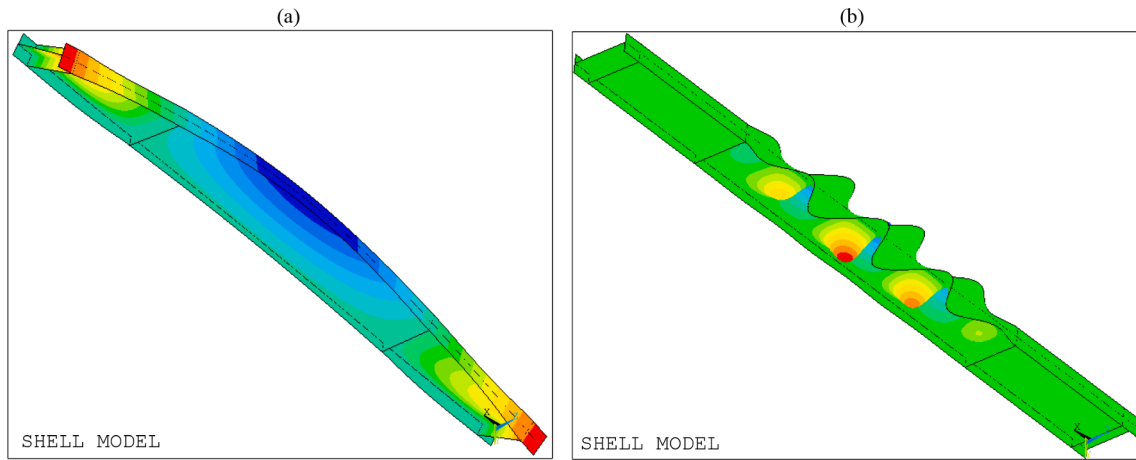
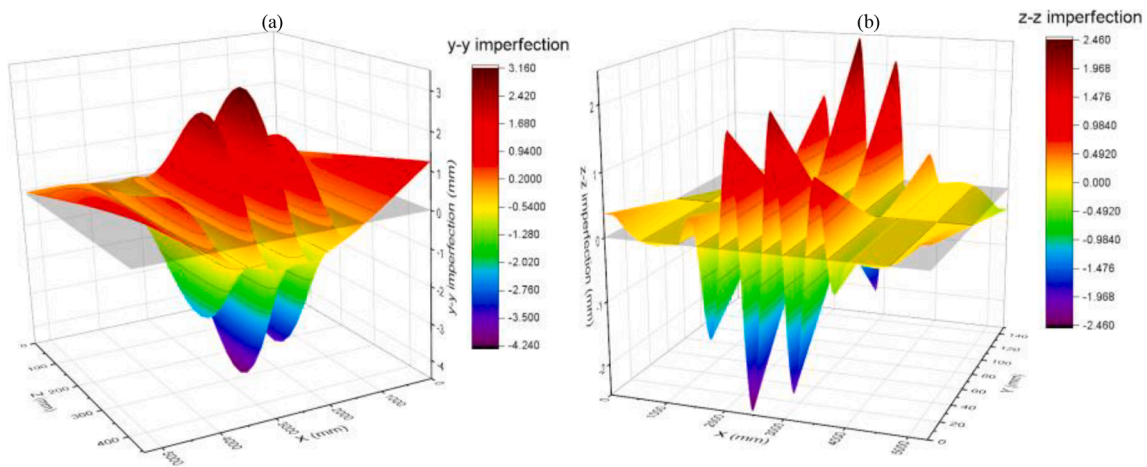**Fig. 32.** ANSYS-SM for Test-1. (a) Global mode shape. (b) Local mode shape.

Fig. 33. (a) Imperfections added to *y*-coordinates of the web for Test-1 (mm). (b) Imperfections added to *z*-coordinates of the top flange for Test-1 (mm).

global and local buckling mode shapes.

The target temperature of the top and bottom flanges and the web in the thermal conditioning phase correspond to the measured temperatures. It is directly specified as a uniform temperature to be attained into the shell elements discretizing each part of the beam. The shell elements representing the stiffeners have the web temperature. In the post-conditioning stage, the controlled displacement mechanical load is directly applied at the top flange nodes on the top edge of the stiffeners until a vertical displacement target value of 22.75 mm is attained. The applied load is shown in Fig. 31b as green displacement boundary conditions. In this phase, measured temperatures are applied to the shell elements representing each part of the beam.

6. Validation of the proposed strategies

The proposed modeling strategies are validated using the experimental results of FIDESC4 Test-1, and Test-3 and compared to the results of the SAFIR and ABAQUS numerical simulations reported in [24].

6.1. Test-1 validation

Fig. 34 shows the total force applied (*P*) versus the beam mid-span vertical deflection (*Uz*) at the bottom flange mid-point for Test-1, FIDESC4 simulations, and the proposed modeling strategies. Fig. 34 also includes the *P-Uz* relationships of the simulations carried out in ANSYS without residual stresses and thermal strains to observe how
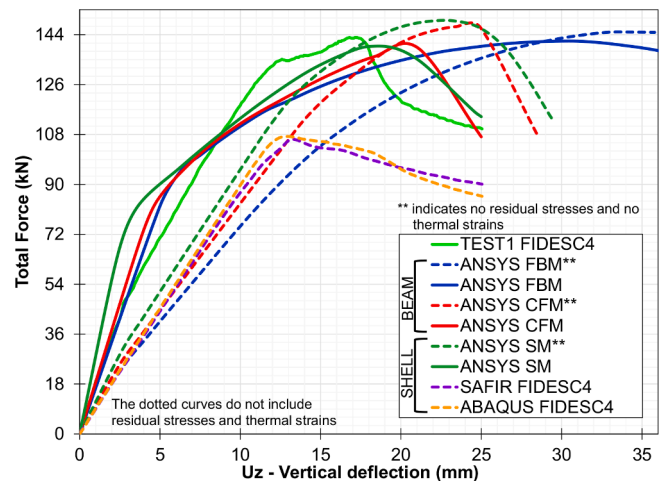
Fig. 34. Total applied load versus vertical deflection at the bottom flange mid-point in the beam mid-span for Test-1.

these affect the force and displacement predictions. The total force *P* acting on the beam is obtained by adding the force in each stiffener. The *P-Uz* curves for Test-1, FIDESC4 simulations, and CFM and SM are drawn up to 25 mm of vertical deflection because it was the maximum deflection reported in the FIDESC4 numerical simulations included in

[24]. The *P-Uz* relationship of the FBM is drawn up to 35 mm because the ultimate load is reached at 31.03 mm. The curves of ANSYS simulations without residual stresses and thermal strains (indicated as FBM**, CFM**, and SM** in Fig. 34) are drawn at deflections higher than 25 mm because they all are advanced from those including them. The total force and vertical deflection results show that both proposed modeling strategies (FBM and CFM) are validated satisfactorily against Test-1 results. Simulation results also reveal that CFM gets better deflection predictions than the FBM. Comparing the results of the FBM and CFM simulations with and without residual stresses and thermal strains shows that it is necessary to include these initial conditions in the GMNIA because they correct the force and deflection predictions, resulting in a *P-Uz* curve closer to the test. Including these initial conditions in the simulations significantly improve the *P-Uz* curve trajectory. It is noted that the predictions of the ANSYS models without residual stresses and thermal deformations underestimate the stiffness for the early force values and overestimate the ultimate load and the deflections. Incorporating these initial conditions is manifested in an additional stiffness towards the first part of the *P-Uz* curve and a decrease of the ultimate load and the ultimate deflection. Since the beam is allowed axial displacement, the extra stiffness may be due to the tensile pre-stressing introduced by the initial thermal strains. The decrease in LTB strength is due to a mixture of the unfavorable effects of residual stresses and the adverse effects of geometric imperfections increased by thermal strains. In conclusion, modeling with residual stresses and thermal strains reproduces the conditions of tested FIDESC4 beams subjected to LTB since these are problems with initial stresses and initial strains.

The ultimate load (P_{ult}) and the ultimate vertical deflection (Uz_{ult}) at the bottom flange mid-point in the beam center from the test, FIDESC4 simulations, and the proposed modeling strategies with and without residual stresses and thermal strains are compared in Table 3. The ultimate cumulative strain energy (E^ε_{ult}) associated with the mechanical work in the beam is also included as a criterion to complement the evaluation of the simulation results. This mechanical work is related to the deformation (elastic and plastic) accumulated until the ultimate load capacity is reached; therefore, ultimate cumulative strain energy (E^ε_{ult}) is calculated as the area under the curve *P* vs. *Uz* up to the ultimate load in Fig. 34. In Table 3, the best result of the two proposed modeling strategies, FBM and CFM, is underlined and bold. It can be seen that CFM adequately predicts both total force and vertical deflection. FBM predicts the ultimate load value well, but its ultimate deflection is larger than the measured, so its ultimate cumulative strain energy is overestimated by 1.13 times regarding the test. It means FBM does not fully represent the beam buckling scenario since the ultimate load occurs at a higher deflection value than the actual one. Table 3 also lists the ultimate flexural moment (M_{ult}) in the heated part of the beam in pure bending, which is calculated as half the ultimate load (½P_{ult}) multiplied by the distance from the end support to the load application point (L2) (see Fig. 5). Again, FBM has a slightly better prediction of M_{ult} than CFM, but CFM better reproduces the structure's response up to the end of the

Table 4
Overestimation of the predictions of the proposed models without residual stresses and thermal strains for Test-1.

	P_{ult} [%]	Uz_{ult} [%]	E^ε_{ult} [%]
ANSYS FBM**	2.34	15.34	3.27
ANSYS CFM**	5.63	18.25	8.14
ANSYS SM**	6.51	18.58	8.66

test.

Table 4 shows the percentage overestimation of P_{ult}, Uz_{ult}, and E^ε_{ult} by the modeling strategies without residual stresses and thermal strains compared to those including them. Not considering these initial conditions in the models leads to overestimates of all three predictions, with the overestimation of the Uz_{ult} being higher. SM** makes the highest overestimates in all three predictions, followed by CFM** and the lowest by FBM**.

Table 5 shows the ratio of Test-1 ultimate moment (M_{ult}) to the elastic bending moment of the section under non-uniform temperature (My_{fire}). The ratio indicates that the buckling limit state controlling failure occurs at an ultimate load (P_{ult}) equal to 46.8% of the elastic load ($P_y = 305.43$ kN).

Fig. 35 compares the buckling shape (failure mode) of Test-1 with those obtained in previous FIDESC4 numerical simulations (Fig. 35e and f) included in [24,29] and with those obtained with the proposed modeling strategies. At the beginning of the experiment, a white-colored grid of 18 equal spaces was drawn on the top flange (in the heated central zone) to evidence the site of the local failure. The experimental deformed shape (Fig. 35a) shows that the local failure in the top flange is offset from the beam mid-span section, i. e., at the end of the first third of the heated zone over the 5th grid line drawn on the top flange. The FBM deformed shape (Fig. 35b) represents the global LTB failure in the heated central part of the beam but cannot capture the local failure shape in the top flange. However, vertical deflection isocontours on the web (blue colored) evidence the high compressions taking place in the failure zone. The CFM deformed shape (Fig. 35c) correctly reproduces the site where the local buckling on the top flange occurs and shows the web local buckling depicted by some web undulations in the middle span and the typical curvature characterizing the global LTB. The local buckling phenomena of the top flange and the web reproduced by CFM and ANSYS-SM are shown in Figs. 35c, d, and 36. Images are practically identical, and both reproduce well the experimental failure,

Table 5
Relationship between the ultimate moment in the heated part of the beam and elastic bending moment.

M^{Test}_{ult} (kN-m)	$My^{Theor.}_{fire}$ [19,21] (kN-m)	$\left\lvert \dfrac{M^{Test}_{ult}}{My^{Theor}_{fire}} \right\rvert$
78.60	167.98	0.468

Table 3
Comparison of results between FIDESC4 simulations, experimental test, and proposed modeling strategies with and without residual stresses and thermal strains.

		P_{ult} (kN)	Uz_{ult} (mm)	E^ε_{ult} (J)	M_{ult} (kN-m)	$\dfrac{P^{Num}_{ult}}{P^{Exp}_{ult}}$	$\dfrac{Uz^{Num}_{ult}}{Uz^{Exp}_{ult}}$	$\dfrac{E^{Num}_{ult}}{E^{Exp}_{ult}}$
BEAM MODELS	TEST 1 FIDESC4	142.96	17.13	1635.63	78.63	—	—	—
	ANSYS FBM**	144.93	35.79	3599.20	79.71	1.01	2.09	2.20
	ANSYS FBM	**141.61**	31.03	3485.31	**77.89**	**0.99**	1.81	2.13
	ANSYS CFM**	146.88	24.95	2322.34	80.79	1.03	1.46	1.42
	ANSYS CFM	139.05	**21.10**	**2147.61**	76.48	**0.97**	**1.23**	1.31
SHELL MODELS	ANSYS SM**	148.96	21.78	2040.44	81.93	1.04	1.27	1.25
	ANSYS SM	139.85	18.37	1877.84	76.92	0.98	1.07	1.15
	ABAQUS SM FIDESC4	107.26	13.02	756.48	58.99	0.75	0.76	0.46
	SAFIR SM FIDESC4	106.26	13.23	757.50	58.44	0.74	0.77	0.46

** indicates that residual stresses and thermal strains are not included. The best result of the two proposed modeling strategies, FBM and CFM, is underlined and bold.
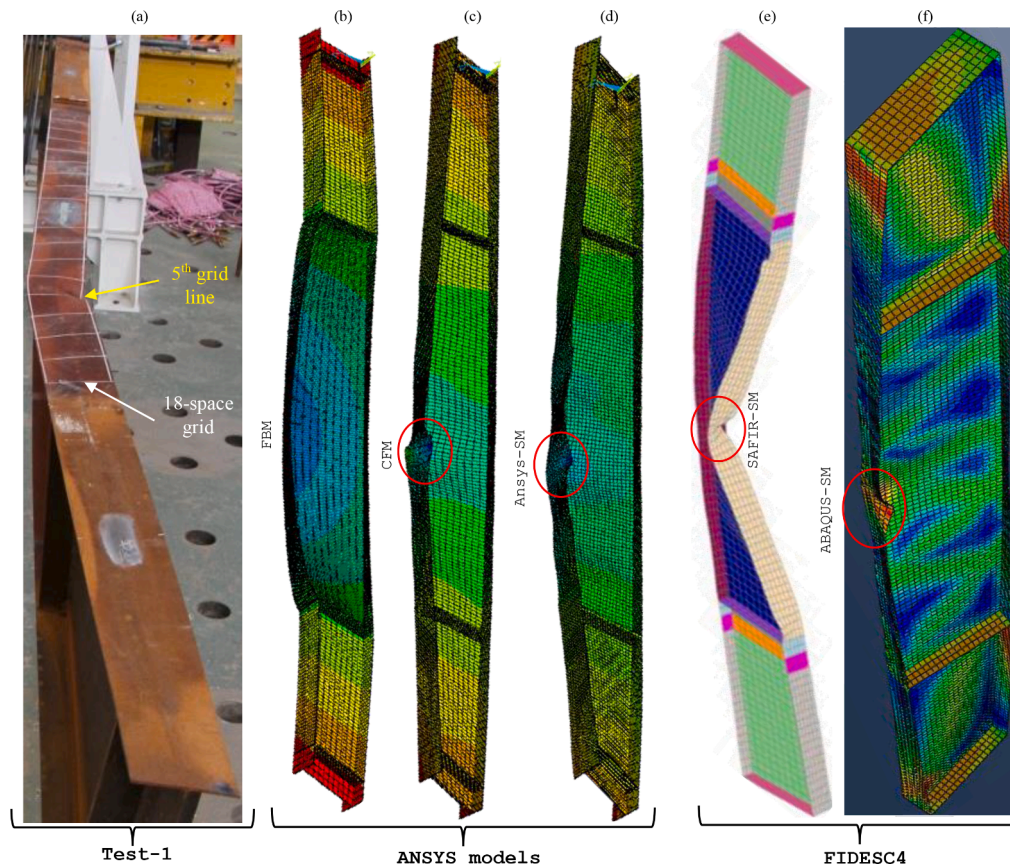
Fig. 35. Deformed shapes of Test-1 models. (a) FBM Uz deflection. (b) CFM Uz deflection. (c) ANSYS-SM Uz deflection (d) FIDESC4 Test-1 [24]. (e) FIDESC4 SAFIR-SM [24]. (f) FIDESC4 ABAQUS-SM [24]
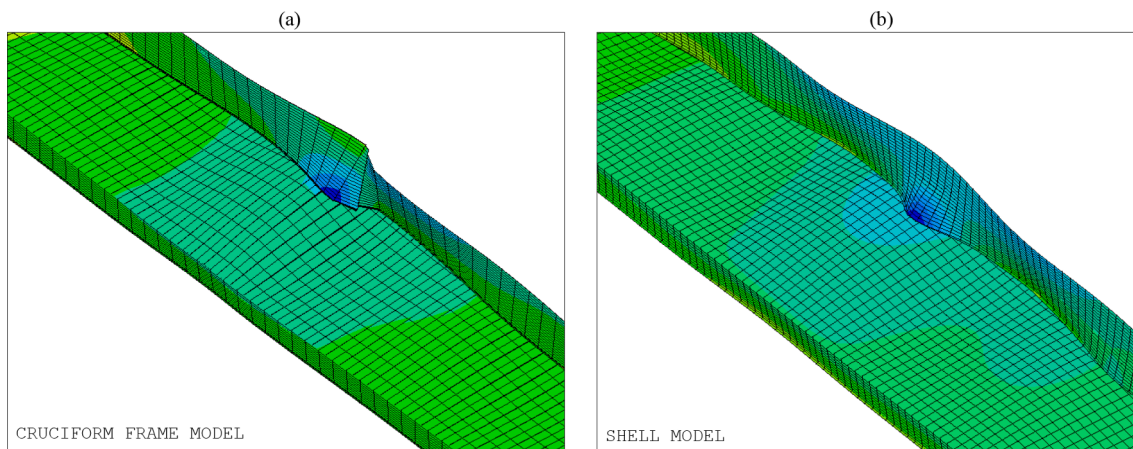

Fig. 36. Top flange and web local buckling detail. (a) CFM. (b) ANSYS-SM.

demonstrating that CFM can correctly reproduce the global and localized LTB failures. The advantage of CFM over ANSYS-SM is its simplicity and the significant reduction of the number of elements used for the discretization, which reduces the computational cost. These advantages (accuracy and simplicity) make CFM a simple and low-cost alternative for simulating LTB in class-4 steel members under fire.

Since the bending generates compression stresses in the top flange and most of the web, the occurrence of tensile stress patterns in these areas demonstrates that some tensile residual stresses remain after the LTB failure. This phenomenon can be observed in Fig. 37, where general and detailed views of the axial stress isocontours at the simulation end time for each ANSYS modeling strategy are shown. The details in

Fig. 37d–f show red and yellow tension stress bands in the top welded zone at the simulation end time, demonstrating the existence of tensile residual stresses in the top compressed part of the beam. Fig. 37 also shows that tensile residual stresses in the top compressed part, in the unheated zone of the beam, are less dissipated than in the heated zone. This behavior indicates that residual stresses should not be neglected in the structural analysis of steel members with class-4 cross-sections under localized fire scenarios where the temperature along the members is non-uniform. On the other hand, the tensile stresses localized on the web come from high web compressions produced by bending that generate buckling in the compressed zone of the web. Thus, the web behaves like a thin, slender plate subjected to compression, causing typical buckling
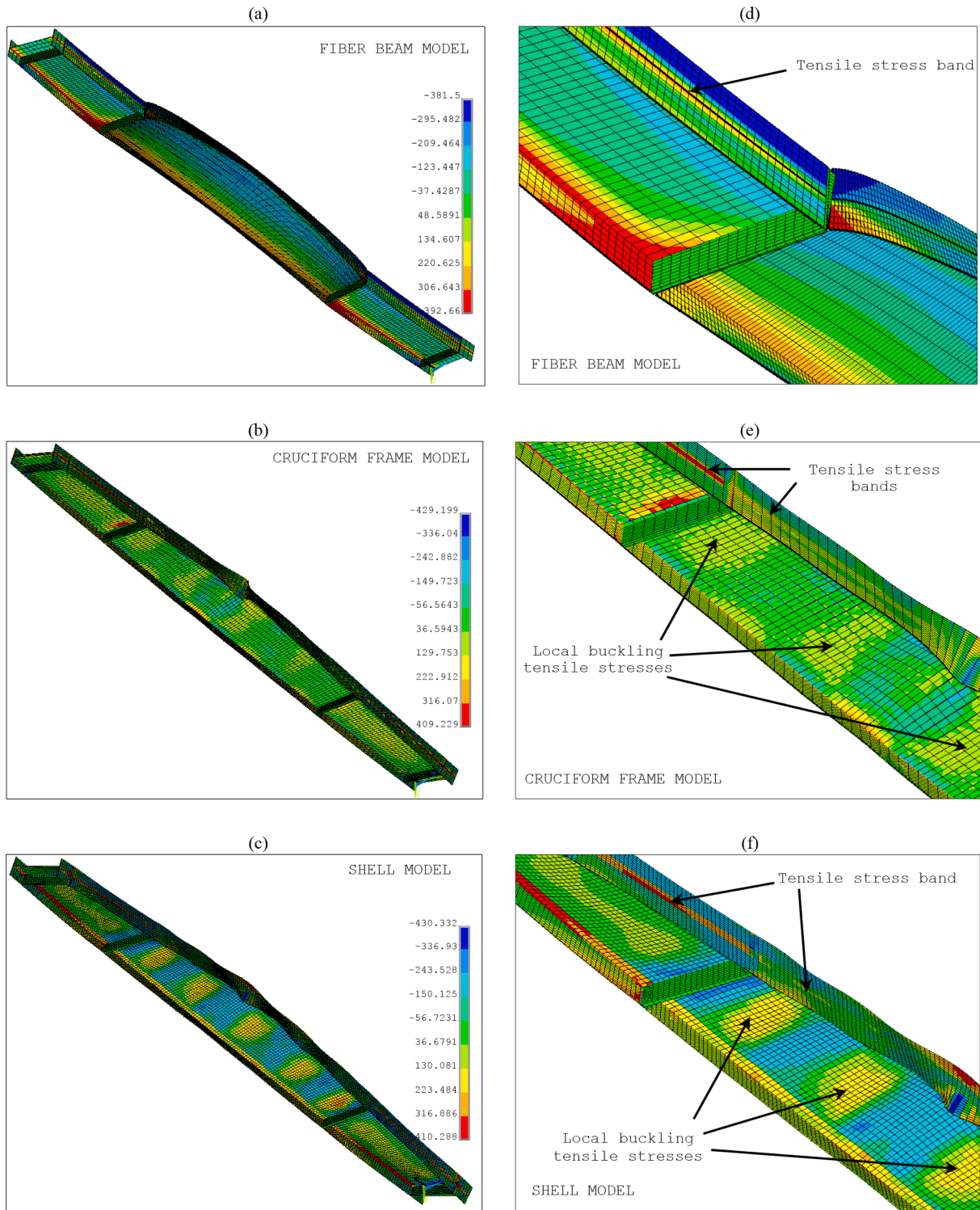
Fig. 37. Axial stresses at the end of the analysis [MPa]. (a,d) FBM. (b,e) CFM. (c,f) ANSYS-SM.

undulations in the longitudinal direction, as shown in Fig. 37e, f. In other words, bending induces local buckling on the web. In Fig. 37, the compressive stresses are negative, and the tensile stresses are positive.

Some additional results at the end of the simulation related to torsional phenomena such as warping, bimoment, and bicurvature are shown in Fig. 38–40. These additional results are given only for FBM because they are easily available from the single fiber representing the tested beam. Figs. 38 and 39 show that the warping degree-of-freedom is

null, and the bicurvature is significant at the beam mid-span where the maximum torsion occurs. The minimum (*MN*) and maximum (*MX*) warping points on the deformed shape (in Fig. 38) match the zero-bicurvature points (see Fig. 39). The changes of sign in the bicurvature diagram of Fig. 39 indicate warped torsion direction changes. The jumps in bicurvature and bimoment diagrams in Figs. 39 and 40 occur by the torsional resistance in the stiffener points. In turn, Fig. 41 shows the bicurvature-bimoment relationship representing the LTB evolution
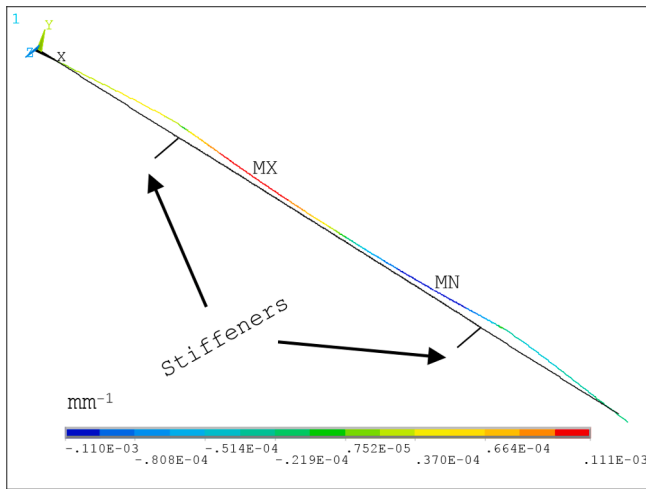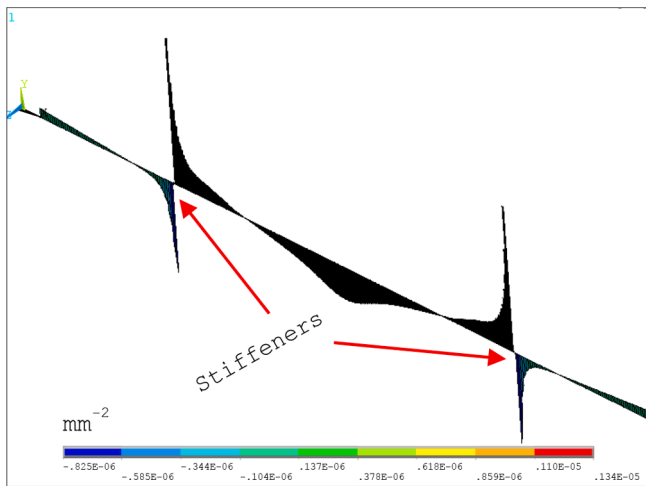
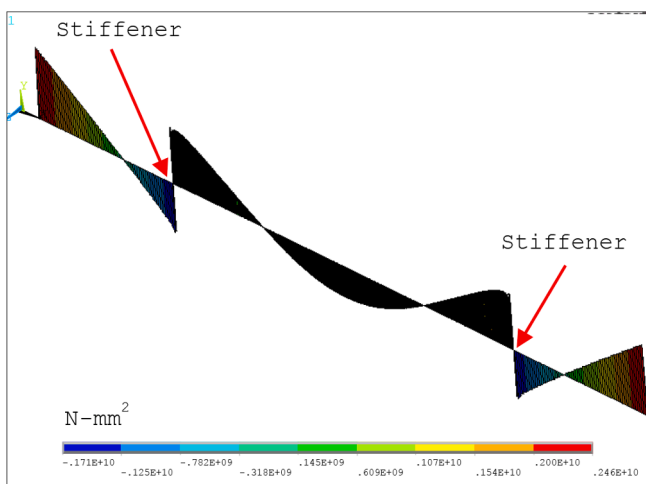**Fig. 38.** Warping on the deformed shape.

Fig. 39. Bicurvature.

Fig. 40. Bimoment.

at mid-span. Initially, the bimoment is negative and then becomes ascending, indicating that the twisting direction of the cross-section changes during the test. The increase of the bimoment in the section is consistent with the LTB failure occurring at the beam mid-span.
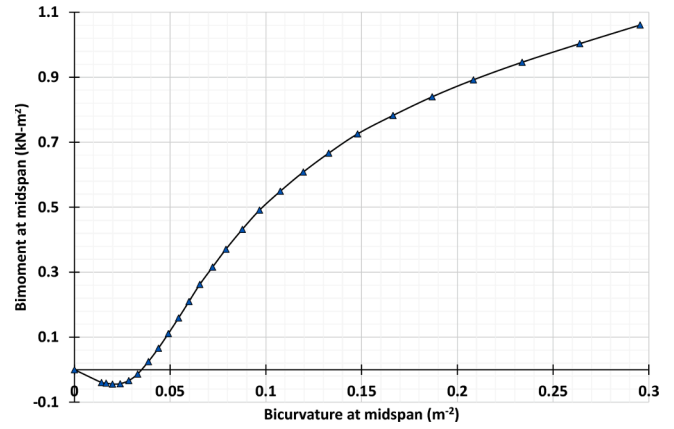

Fig. 41. Bimoment-bicurvature relationship.

Although FBM cannot capture the local failure shape in the top flange, torsional results show that it simulates well the LTB phenomenon.

6.2. Test-3 validation

Fig. 42 shows the total force applied (*P*) versus the beam mid-span vertical deflection (*Uz*) at the bottom flange mid-point for Test-3, FIDESC4 simulations, and the proposed modeling strategies. Fig. 42 also presents the *P-Uz* curves of the simulations carried out in ANSYS without residual stresses and thermal strains. The *P-Uz* curves for Test-3, FIDESC4 simulations, and CFM and SM are drawn up to 30 mm of vertical deflection according to FIDESC4 numerical simulations reported in [24]. The *P-Uz* relationship of the FBM is drawn past 35 mm because the ultimate load is only reached at 35.03 mm. The curves of ANSYS simulations without residual stresses and thermal strains are drawn at deflections higher than 30 mm because they are advanced from those including them. Results indicate that the two proposed modeling strategies (FBM and CFM) validate satisfactorily against Test-3. Once more, CFM gets better deflection predictions than the FBM. Moreover, predictions of the ANSYS models without residual stresses and thermal deformations again tend to underestimate the stiffness for the early force values and overestimate the ultimate load and defections. All other comments presented in Test-1validation are confirmed in Test-3 validation.

In Table 6, the best result of the two proposed modeling strategies, FBM and CFM, is underlined and bold. Once again, FBM predicts the ultimate load value well, but its ultimate deflection is larger than the
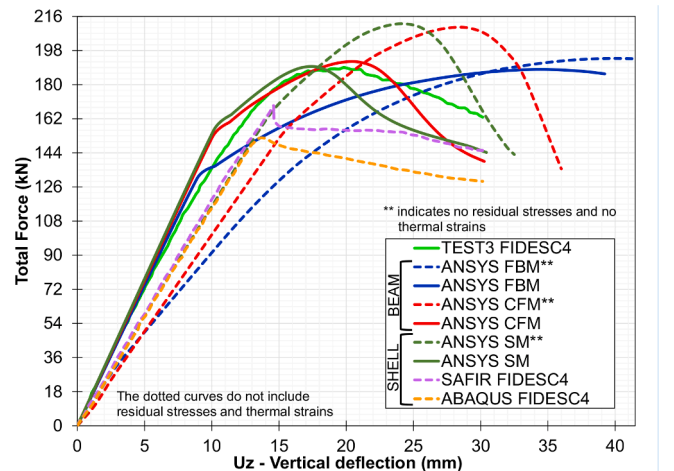

Fig. 42. Total applied load versus vertical deflection at the bottom flange mid-point in the beam mid-span for Test-3.

Table 6
Comparison of results between FIDESC4 simulations, experimental test, and proposed modeling strategies with and without residual stresses and thermal strains.

		P_{ult} (kN)	Uz_{ult} (mm)	E^{ε}_{ult} (J)	M_{ult} (kN-m)	$\dfrac{P^{Num}_{ult}}{P^{Exp}_{ult}}$	$\dfrac{Uz^{Num}_{ult}}{Uz^{Exp}_{ult}}$	$\dfrac{E^{Num}_{ult}}{E^{Exp}_{ult}}$
	TEST 3 FIDESC4	189.06	19.82	2410.10	103.99	—	—	—
BEAM MODELS	ANSYS FBM**	193.82	39.99	5397.66	106.60	1.03	2.02	2.24
	ANSYS FBM	**188.03**	35.06	5040.72	**103.42**	**0.99**	1.77	2.09
	ANSYS CFM**	210.01	29.04	3794.94	115.50	1.11	1.47	1.57
	ANSYS CFM	192.01	**20.85**	**2684.44**	105.61	1.02	**1.05**	**1.11**
SHELL MODELS	ANSYS SM**	212.15	24.31	3125.80	116.68	1.12	1.23	1.30
	ANSYS SM	189.23	17.91	2165.47	104.07	1.00	0.90	0.90
	ABAQUS SM FIDESC4	151.95	13.71	1075.23	83.57	0.80	0.69	0.45
	SAFIR SM FIDESC4	168.92	14.60	1263.17	92.91	0.89	0.74	0.52

**Indicates that residual stresses and thermal strains are not included. The best result of the two proposed modeling strategies, FBM and CFM, is underlined and bold.

Table 7
Overestimation of the predictions of the proposed models without residual stresses and thermal strains for Test-3.

	P_{ult} [%]	Uz_{ult} [%]	E^{ε}_{ult} [%]
ANSYS FBM**	3.08	14.07	7.08
ANSYS CFM**	9.37	39.27	41.37
ANSYS SM**	12.11	35.71	44.35

measured. FBM also has a slightly better prediction of M_{ult} than CFM, but CFM better reproduces the structure's response up to the end of the test. Finally, Table 7 shows the percentage overestimation of P_{ult}, Uz_{ult}, and E^{ε}_{ult} by the modeling strategies without residual stresses and thermal strains. Again, it is found that not considering these initial conditions in the simulations leads to overestimating all three predictions. SM** and CFM** make the highest overestimations for Uz_{ult} and E^{ε}_{ult}.

All discussions given of the simulation results of Test-1 are confirmed in the validation of Test-3, demonstrating that the proposed modeling strategies correctly simulate the LTB response of steel members with class-4 cross-sections under fire conditions with constant cross-section. On the other hand, the ratio of Test-3 ultimate moment (M_{ult}) to the elastic bending moment of the section under non-uniform temperature (My_{fire}) shown in Table 8 points out that the buckling limit state controlling failure occurs at an ultimate load (P_{ult}) equal to 45.4% of the elastic load (P_y = 416.56 kN).

Fig. 43 compares the buckling shape (failure mode) of Test-3 with those obtained in previous FIDESC4 numerical simulations (Fig. 43e and f) included in [24,29] and with those obtained with the proposed modeling strategies. The experimental deformed shape (Fig. 43a) shows that the local failure in the top flange is near the beam mid-span section, i.e., over the 9th grid line drawn on the top flange. The FBM deformed shape (Fig. 43b) reproduces the global LTB failure in the heated central part of the beam but cannot capture the local failure shape in the top flange while the CFM deformed shape (Fig. 43c) correctly reproduces the place where local buckling occurs. The CFM deformed shape resembles that of ANSYS-SM (Fig. 43d) and accurately represents the web undulations in the central part of the beam and the local buckling of the top flange. Details of the failure mode for CFM and ANSYS-SM evidencing their similarity are shown in Fig. 44.

Finally, the CPU times spent for each modeling strategy to carry out the full-GMNIA in ANSYS for Test-1 and Test-3, are shown in Fig. 45. It can be seen that the best computation time is for CFM due to the reduction in the degrees of freedom and the complexity level achieved

by discretizing with BEAM189 elements making it the best alternative to model the LTB problem in class-4 beams. In Fig. 45, the number of nodes, elements, and degrees of freedom is related to the CPU. For example, in Test-1 (Fig. 45a), it is observed that correct results can be achieved with a low-cost CFM of 2488 BEAM189 finite elements, 3413 nodes, and 23,891 degrees of freedom instead of a high-cost SM of 14,596 SHELL181 finite elements, 14,789 nodes, and 88,734 degrees of freedom. In Test-3 (Fig. 45b), the CFM nodes are slightly high (2508), whereas SM is still the same size. The time reduction of CFM versus SM is 52.2% in Test-1 and 46.7% in Test-3. Low-cost of CFM is caused by the quadratic interpolation of the BEAM189 finite element, which reduces the number of elements without losing the accuracy of results. On the other hand, the high refinement requirements in the cross-section pseudo-mesh to achieve the accuracy of the ultimate load increase the FBM computational cost, penalizing the advantage achieved by saving the number of elements making it the highest computational cost. CPU times are calculated in ANSYS using parallel distributed memory-MPI calculation in 6 physical cores on a Dell Mobile Workstation 7530/64 bits, Intel Xeon Processor-2.71 GHz, and Ram-32 GB.

7. Conclusions and future work

This paper proposes two new methodologies implemented in ANSYS to predict the LTB strength in steel beams with class-4 cross-sections subjected to fire action. The procedures use beam-type finite elements with the Timoshenko formulation and are based on a GMNIA that includes imperfections, residual stresses, and thermal strains. In the first modeling strategy (FBM), the beam is represented by a beam-type finite element fiber. In the second modeling strategy (CFM), the beam is represented by a beam-type finite element grid arrangement. Both modeling strategies are validated with experimental and numerical simulations of Test-1 and Test-3 carried out in the FIDESC4 [24] investigation on a slender beam of class-4 section and with a specific shell model of the same test built whit ANSYS. In all three cases, the validation of the ultimate load capacity of both tests was satisfactory. From the studies performed, the following conclusions can be drawn:

– Both methodologies correctly predict the ultimate load of the class-4 steel members under fire and avoid using more complex finite element models. This simplification of the structural model is an important advantage over strategies that use shell elements (see, e.g., those included in [36,37]) and allows for full 3D analyses adapted to the 3D nature of the LTB phenomenon in real beams.
– The FBM strategy discretizes the steel member using a fiber representing the beam axis located at the outer edge of the beam where the boundary conditions are applied. Two types of elements are used to build the model: BEAM189 elements to model the fiber axis and LINK180 elements to transfer the load from the application points to the fiber axis representing the beam. FBM correctly predicts the ultimate load and is easy to build, and the number of elements and model building time is small, which is useful for quickly building

Table 8
Relationship between the ultimate moment in the heated part of the beam and elastic bending moment.

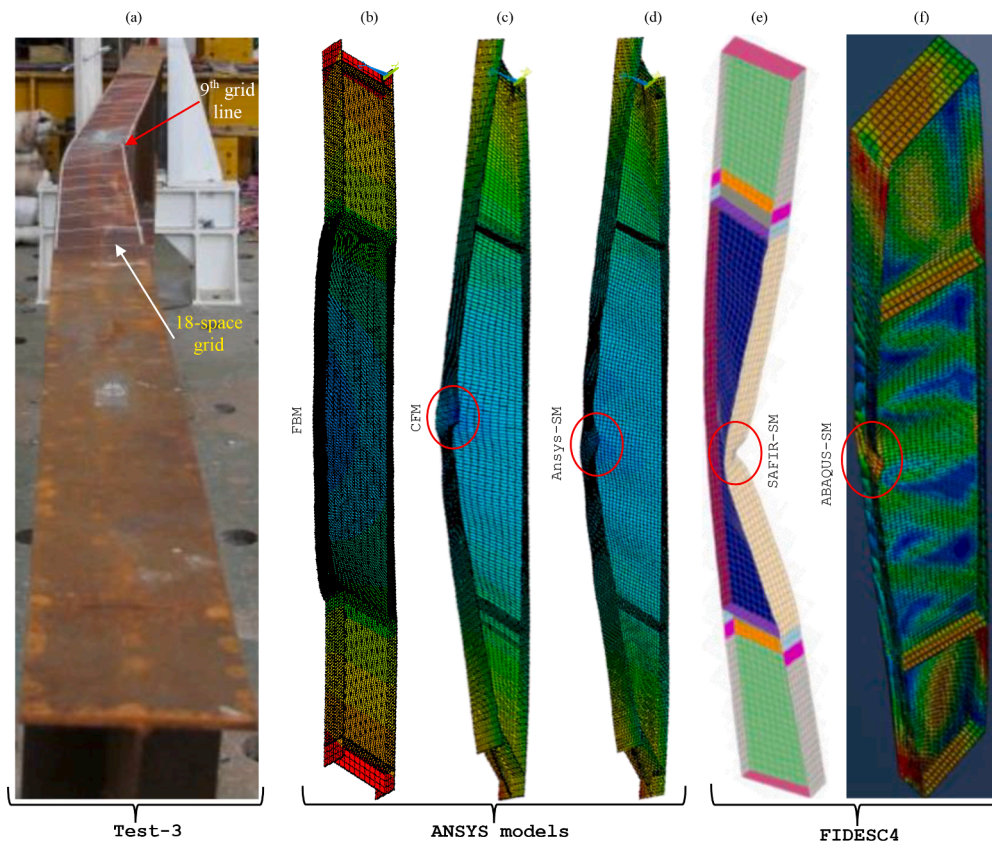| M^{Test}_{ult} (kN-m)	$My^{Theor.}_{fire}$ [19,21] (kN-m)	$\left|\dfrac{M^{Test}_{ult}}{My^{Theor}_{fire}}\right|$
103.99	229.11	0.454

Fig. 43. Deformed shape of Test-3 models. (a) FBM Uz deflection. (b) CFM Uz deflection. (c) ANSYS-SM Uz deflection (d) FIDESC4 Test-3 [24]. (e) FIDESC4 SAFIR-SM [24]. (f) FIDESC4 ABAQUS-SM [24]
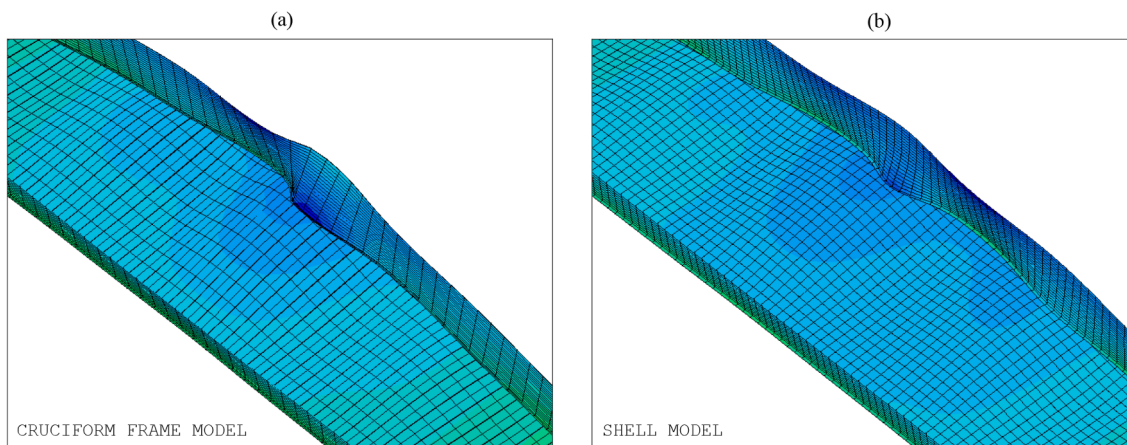

Fig. 44. Top flange and web local buckling detail. (a) CFM. (b) ANSYS-SM.

multi-member models. Furthermore, its nodal results are easy to process. Although FBM is easier to build than CFM, its main disadvantages are that (a) FBM does not reproduce the local buckling shape and (b) FBM has a higher computational cost than CFM. Therefore, its use is not recommended for (a) post-buckling performance analyses and for (b) LTB analyses in steel beams requiring a large number of simulations as it would be the case of probabilistic and optimization analyses and involving knowledge of the collapse load. However, FBM can be very useful when the designer is interested only in the ultimate load as in the LTB analysis under fire of multi-member steel structures belonging to industrial facilities or building frames.

– The CFM strategy discretizes the web and flanges of the steel member using a cruciform arrangement of BEAM189 element fibers to capture local buckling. This strategy is proposed to simplify the construction and reduce the computational cost of the shell models typically used for LTB analyses. CFM correctly predicts the structural response, the ultimate load, and even the local buckling failure of the tested beams. In addition, it is simpler, less computationally expensive than shell models. This reduction in computational cost opens the path for a wider application of probabilistic models to complex structures under fire and represents a significant step towards the generalized application of performance-based approaches to address fire effects. Therefore, CFM is recommended for evaluating the
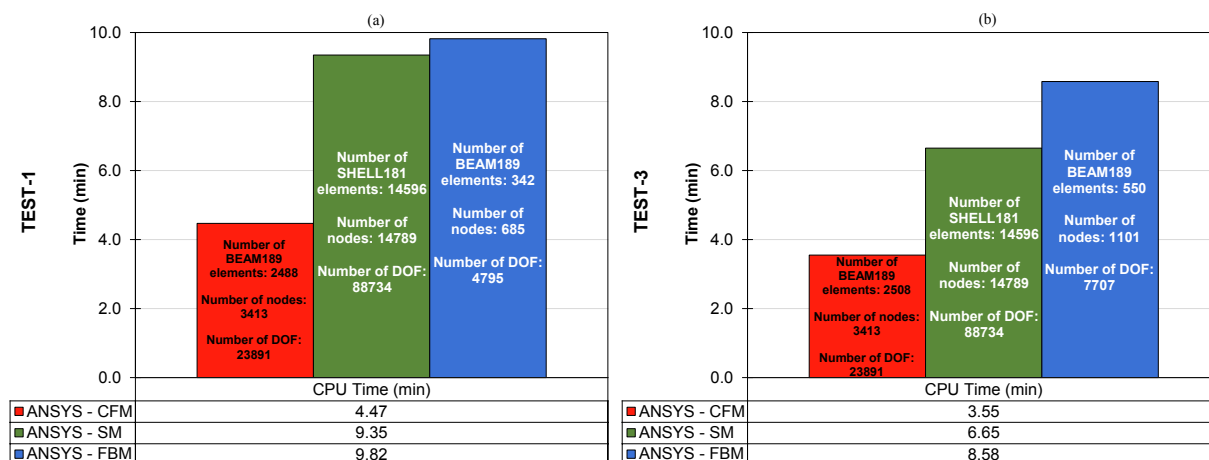
Fig. 45. Comparison of the CPU times of the proposed modeling strategies. (a) Test-1. (b) Test-3.

complete performance of the structure up to the collapse, as well as for optimization and probabilistic analyses.

– The simulation of the configuration and the conditions of the FIDESC4 experiments in slender beams of class-4 cross-section at high temperatures constitutes a modeling problem where initial stresses and initial strains are present. Therefore, both are indispensable for the proper calculation of the global response to the problem. The results of simulations carried out to validate the tests with and without residual stresses and thermal strains point out that the inclusion of these two initial conditions favorably modifies the LTB response of the tested beams. As a result, substantial improvements are evident in the evaluation of the initial stiffness of the beams and also in the calculations of ultimate load, ultimate displacement, and strain energy accumulated up to the ultimate load. In addition, it was verified that some tensile residual stresses remained after LTB failure, especially in the unheated part of the beam. This is another reason for including them in the LTB analysis of class-4 steel members in localized fire scenarios where the temperature along the member is not uniform

– This study verified that the class-4 steel member strength under fire is significantly smaller than its elastic strength because buckling appears early [19,21]. In both tests, the buckling limit state established the ultimate load (P_{ult}) at approximately 46% of the theoretical elastic load (P_y).

– Future works should be addressed to adapt these modeling strategies to: (1) the analysis of lateral-torsional buckling in steel beams (with variable cross-section), (2) the analysis of torsional flexural buckling phenomena in steel columns (with constant and variable cross-sections) as a previous step to their implementation in the analysis of complete frames, (3) the optimization and probabilistic design of class-4 steel members under fire.

CRediT authorship contribution statement

Myriam R. Pallares-Muñoz:,**Ignacio Payá-Zaforteza:**,**Antonio Hospitaler-Pérez:**.

Declaration of Competing Interest

The authors declare that they have no known competing financial interests or personal relationships that could have appeared to influence the work reported in this paper.

Acknowledgments

References

[1] Elkawas AA, Hassanein MF, El Hadidy AM, El-Boghdadi MH, Elchalakani M. Behaviour of corrugated web girders subjected to lateral-torsional buckling: Experimental tests and numerical modelling. Structures 2021;33:152–68. https://doi.org/10.1016/j.istruc.2021.04.057.

[2] Arcelormittal. Dusseldorf`s iconic Kö-Bogen. 2014.

[3] Arcelormittal. Wirkowise composite bridge: Europe's first road bridge with Arcorox weathering steel. 2020.

[4] Yoders J. Chicago's Union Station Tower Uses First 80-ksi Steel Sections in the US. ENRMidwest 2020.

[5] Shahbazian YWMMA. Fire performance of thin-walled steel structures. 1st ed. London: CRC Press; 2020.

[6] Qin C. Collapse simulations of steel buildings under fire. Colorado State University, 2016.

[7] Qin C, Mahmoud H. Collapse performance of composite steel frames under fire. Eng Struct 2019;183:662–76. https://doi.org/10.1016/j.engstruct.2019.01.032.

[8] Shakib H, Zakersalehi M, Jahangiri V, Zamanian R. Evaluation of Plasco Building fire-induced progressive collapse. Structures 2020;28:205–24. https://doi.org/10.1016/j.istruc.2020.08.058.

[9] Ahmadi MT, Aghakouchak AA, Mirghaderi R, Tahouni S, Garivani S, Shahmari A, et al. Collapse of the 16-Story Plasco Building in Tehran due to Fire. Fire Technol 2020;56(2):769–99. https://doi.org/10.1007/s10694-019-00903-y.

[10] Wright W, Lattimer B, Woodworth M, Nahid M, Sotelino E. Highway bridge fire assessment draft final report. Blacksburg: 2013.

[11] Alos-Moya J, Paya-Zaforteza I, Garlock MEM, Loma-Ossorio E, Schiffner D, Hospitaler A. Analysis of a bridge failure due to fire using computational fluid dynamics and finite element models. Eng Struct 2014;68:96–110. https://doi.org/10.1016/j.engstruct.2014.02.022.

[12] Peris-Sayol G, Paya-Zaforteza I, Balasch-Parisi S, Alós-Moya J. Detailed Analysis of the Causes of Bridge Fires and Their Associated Damage Levels. J Perform Constr Facil 2017;31(3):04016108. https://doi.org/10.1061/(ASCE)CF.1943-5509.0000977.

[13] Garlock M, Paya-Zaforteza I, Kodur V, Gu Li. Fire hazard in bridges: Review, assessment and repair strategies. Eng Struct 2012;35:89–98. https://doi.org/10.1016/j.engstruct.2011.11.002.

[14] Payá-Zaforteza I, Garlock MEM. A numerical investigation on the fire response of a steel girder bridge. J Constr Steel Res 2012;75:93–103. https://doi.org/10.1016/j.jcsr.2012.03.012.

[15] Szychowski A, Brzezińska K. Local Buckling and Resistance of Continuous Steel Beams with Thin-Walled I-Shaped Cross-Sections. Appl Sci 2020;10(13):4461. https://doi.org/10.3390/app10134461.

[16] CEN. EN 1993-1-2. Eurocode 3: Design of steel structures - Part 1-2: General rules - Structural fire design. Brussels: European Committee for Standardization; 2005.

[17] Mohri F, Brouki A, Roth JC. Theoretical and numerical stability analyses of unrestrained, mono-symmetric thin-walled beams. J Constr Steel Res 2003;59(1):63–90. https://doi.org/10.1016/S0143-974X(02)00007-X.

[18] Seres N, Fejes K. Lateral-torsional buckling of girders with class 4 web: Investigation of coupled instability in EC3-based design approach. Adv Struct Eng 2020;23(11):2442–57. https://doi.org/10.1177/1369433220915623.

[19] Kulak L, Grondin GY. Limit States Design In Structural Steel. 10th ed. Canadian Institute of Steel Construction; 2018.

[20] Schmidt H. Stahlbaunormen: Kommentar zu DIN EN 1993-1-6: Festigkeit und Stabilität von Schalen. Stahlbau-Kalender-Tag 2012, Stuttgart: Universität Stuttgart. Institut für Konstruktion und Entwurf; 2013. www.p-s-p.de/uploads/downloads/Vortrag_Schmidt_Kommentar_zu_DIN_EN_1993-1-6_Stuttgart_2012-06.pdf.

[21] Buchanan A, Abu A. Steel Structures. Struct. Des. Fire Saf. New Zealand: John Wiley & Sons, Ltd; 2016. p. 154–94. https://doi.org/10.1002/9781118700402. ch6.

[22] Axhag F. Plastic design of steel bridge girders. Luleå tekniska universitet 1998.

[23] Thiébaud R, Lebet J-P. Lateral Torsional Buckling of steel bridge girders. Proc Annu Stab Conf SSCR n.d.:1–19.

[24] Wald F, František J-M, Vila Real P, Oly R, Zhao B, Morente F, Velda P. Fire design of steel members with welded or hot-rolled class 4 cross-section (FIDESC4). 2014th ed. Luxembourg: RFSC Publications; 2016. https://doi.org/10.2777/33944.

[25] Agüero A, Baláž I, Koleková Y. New method for metal beams sensitive to lateral torsional buckling with an equivalent geometrical UGLI imperfection. Structures 2021;29:1445–62. https://doi.org/10.1016/j.istruc.2020.11.047.

[26] Quiel SE, Moreyra Garlock ME, Paya-Forteza I. Closed-Form Procedure for Predicting the Capacity and Demand of Steel Beam-Columns under Fire. J Struct Eng 2011;137(9):967–76. https://doi.org/10.1061/(ASCE)ST.1943-541X.0000443.

[27] Yang K-C, Lee H-H, Chan O. Performance of steel H columns loaded under uniform temperature. J Constr Steel Res 2006;62(3):262–70. https://doi.org/10.1016/j.jcsr.2005.07.001.

[28] Heidarpour A, Bradford MA. Local buckling and slenderness limits for flange outstands at elevated temperatures. J Constr Steel Res 2007;63(5):591–8. https://doi.org/10.1016/j.jcsr.2006.07.007.

[29] Prachar M, Jandera M, Wald F, Zhao B. Lateral torsional-buckling of class 4 steel plate beams at elevated temperature: Experimental and numerical comparison. 2014. fire.fsv.cvut.cz/fidesc4/Prachar-validation.pdf.

[30] Prachar M, Jandera M, Wald F, Zhao B. Lateral torsional-buckling of class 4 steel plate beams at elevated temperature: Experimental and numerical comparison. J Struct Fire Eng 2015. https://doi.org/10.1260/2040-2317.6.3.223.

[31] Prachar M, Jandera M, Wald F, Zhaob B. Fire resistance of slender section beams. Steel Constr 2014;7(3):188–92. https://doi.org/10.1002/stco.v7.310.1002/stco.201410031.

[32] Couto C, Vila Real P, Lopes N, Zhao B. Numerical investigation of the lateral-torsional buckling of beams with slender cross sections for the case of fire. Eng Struct 2016;106:410–21. https://doi.org/10.1016/j.engstruct.2015.10.045.

[33] Jandera M, Prachař M, Wald F. Lateral-torsional buckling of class 4 section uniform and web tapered beams at elevated temperature. Thin-Walled Struct 2020;146: 106458. https://doi.org/10.1016/j.tws.2019.106458.

[34] Kucukler M, Gardner L, Macorini L. Lateral–torsional buckling assessment of steel beams through a stiffness reduction method. J Constr Steel Res 2015;109:87–100. https://doi.org/10.1016/j.jcsr.2015.02.008.

[35] Šorf M, Jandera M. Lateral-torsional buckling of slender cross-section stainless steel beams. Structures 2020;28:1466–78. https://doi.org/10.1016/j.istruc.2020.09.073.

[36] Nguyen XT, Park JS. Nonlinear Buckling Strength of Steel H-Beam under Localized Fire and Pure Bending. KSCE J Civ Eng 2021;25(2):561–73. https://doi.org/10.1007/s12205-020-0291-z.

[37] Kucukler M. Lateral instability of steel beams in fire: Behaviour, numerical modelling and design. J Constr Steel Res 2020;170:106095. https://doi.org/10.1016/j.jcsr.2020.106095.

[38] Pallares-Muñoz MR, Paya-Forteza I, Hospitaler A. A new methodology using beam elements for the analysis of steel frames subjected to non-uniform temperatures due to fires. Structures 2021;31:462–83. https://doi.org/10.1016/j.istruc.2021.02.008.

[39] Hambly EC. Bridge Deck Behaviour. 2nd ed. Second edi. London: CRC Press; 2014.

[40] Smyrnaios SV, Iliopoulos A, Vayas I. Truss models for inelastic stability analysis and design of steel plate girders. Eng Struct 2015;105:165–73. https://doi.org/10.1016/j.engstruct.2015.09.040.

[41] Ioannis Vayas John Ermopoulos GI. Design of Steel Structures to Eurocodes. 1st ed. Springer International Publishing; 2019.

[42] Possidente L, Tondini N, Battini J-M. 3D Beam Element for the Analysis of Torsional Problems of Steel-Structures in Fire. J Struct Eng 2020;146(7):04020125. https://doi.org/10.1061/(ASCE)ST.1943-541X.0002665.

[43] Franssen J, Cowez B, Gernay T. Effective stress method to be used in beam finite elements to take local instabilities into account. Fire Saf Sci 2014;11:544–57.

[44] Maraveas C, Gernay T, Franssen J-M. An equivalent stress method to account for local buckling in beam finite elements subjected to fire. J Struct Fire Eng 2019;10 (3):340–53. https://doi.org/10.1108/JSFE-09-2018-0020.

[45] Maraveas C, Gernay T, Franssen J-M. Sensitivity of elevated temperature load carrying capacity of thin-walled steel members to local imperfections. Appl Struct Fire Eng – ASFE 2017, Manchester: 2017. doi:10.1201/9781315107202-4.

[46] Maraveas C, Gernay T, Franssen J-M. Buckling of steel plates at elevated temperatures: Theory of perfect plates vs Finite Element Analysis. CONFAB 2017–2nd Int Conf Struct Saf Under Fire Blast Load, London 2017.

[47] Maraveas C, Gernay T, Franssen J-M. Thin-walled steel members at elevated temperatures considering local imperfections: Numerical simulation of isolated plates. 9th Natl. Congr. Met. Struct., Larisa, Greece: 2017.

[48] Wang W, Kodur V, Yang X, Li G. Experimental study on local buckling of axially compressed steel stub columns at elevated temperatures. Thin-Walled Struct 2014; 82:33–45. https://doi.org/10.1016/j.tws.2014.03.015.

[49] Ansys. ANSYS Engineering Analysis System. User manual. Canonsburg, Pennsylvania: Houston, Pa. : Swanson Analysis Systems; 2019.

[50] Oñate E. Structural Analysis with the Finite Element Method Linear Statics: Volume 2. Beams, Plates and Shells. 1st ed. Barcelona: Springer; 2013.

[51] Ansys Inc. ANSYS Mechanical Training Materials. Cust Train Mater 2010; December.

[52] Purkiss JA, Li LY. Fire safety engineering design of structures. 3rd Ed. Boca Raton: CRC Press; 2013. https://doi.org/10.1201/b16059.

[53] Oñate E. Structural Analysis with the Finite Element Method. Linear Statics: Volume 1: Basis and Solids (Lecture Notes on Numerical Methods in Engineering and Sciences) (v. 1). 1st ed. Barcelona: CIMNE; 2009.

[54] ECCS-CECM-EKS. Ultimate Limit State Calculation Of Sway Frames With Rigid Joints. ECCS Publ No33 1984.

[55] Gere JM, Timoshenko SP. Mechanics of Materials. 3rd ed. London, United Kingdom: Springer International Publishing; 1991. https://doi.org/10.1007/978-1-4899-3124-5.